FINAL REPORT FOR
CALIBRATED SYNTHETIC APERTURE SONAR

DEREK R. OLSON AND DANIEL C. BROWN

Current high-frequency synthetic aperture sonar (SAS) imaging systems and processing software have been largely successful in producing high-quality imagery in a variety of oceanographic and seafloor environments. In most high-frequency real aperture and SAS systems, the image pixel values have been adjusted for optimal viewing by operators. The dynamic range of the pixel values may be truncated and the mean background level may vary from image to image, even across images of the same geographic area. Automated Target Recognition (ATR) algorithms that process these images require that pixel energy levels are normalized to remove systematic variations in amplitude that can cause these algorithms to fail. However, the adaptive nature of image normalization algorithms can introduce artifacts as well. In many cases the discarded original pixel values may contain valuable information. Calibrated SAS images, defined as images whose pixel values represent only the scattering properties of the seafloor or target, present a promising input to ATR because 1) they preserve amplitude information, which may provide stable feature measurements to ATR, and 2) they can be normalized without artifacts by taking into account propagation and scattering physics, potentially offering a superior method than current normalization techniques.

For this grant, measured system parameter were used to form calibrated images from a high frequency synthetic aperture sonar system. Systems with large bandwidth and wide beams cannot directly estimate the scattering cross section, since that quantity is defined using a plane wave of a single frequency for the incident field. Correspondingly, the quantities produced by calibrated images must be understood as quantities averaged over the systems bandwidth and beamwidth. Details of this method, and scattering cross section results are presented in the enclosed OCEANS2019 conference paper entitled "Analysis of Backscatter Measurements from Calibrated Synthetic Aperture Sonar Images" by Peter D. Romain, Derek R. Olson, and J. Tory Cobb.

Another aspect explored in this grant is to determine whether the scattering cross section estimated using a broadband system is independent of the system resolution, or bandwidth over which the system forms the image. To answer this question, a numerical method was developed using the Helmholtz integral theorem and Fourier synthesis to estimate the scattering cross section in the time domain from a finite ensemble of rough surfaces. This work is detailed in the enclosed manuscript that was submitted to the Journal of the Acoustical Society of America, entitled "Resolution dependence of rough surface scattering using a power law roughness spectrum" by Derek R. Olson and Anthony P. Lyons.

REPORT DOCUMENTATION PAGE

Form Approved
OMB No. 0704-0188

1. REPORT DATE *(DD-MM-YYYY)*	**2. REPORT TYPE**	**3. DATES COVERED** *(From - To)*
30/10/2019	Final Technical Report	01 Aug 2016 - 31 July 2019

4. TITLE AND SUBTITLE Calibrated SAS: Relevance to ATR and Effects of Variability	**5a. CONTRACT NUMBER**
	5b. GRANT NUMBER N00014-16-1-3039
	5c. PROGRAM ELEMENT NUMBER
6. AUTHOR(S) Dr. Daniel C. Brown	**5d. PROJECT NUMBER** 24638
	5e. TASK NUMBER
	5f. WORK UNIT NUMBER
7. PERFORMING ORGANIZATION NAME(S) AND ADDRESS(ES) The Pennsylvania State University Applied Research Labotatory Office of Sponsored Programs 110 Technology Center Building University Park, PA 16802-7000	**8. PERFORMING ORGANIZATION REPORT NUMBER**
9. SPONSORING/MONITORING AGENCY NAME(S) AND ADDRESS(ES) ONR Ocean Sensing & Systems Apps Div Office of Naval Research 875 North Randolph Street Arlington, VA 22203-1995	**10. SPONSOR/MONITOR'S ACRONYM(S)** ONR
	11. SPONSORING/MONITORING AGENCY REPORT NUMBER

12. DISTRIBUTION AVAILABILITY STATEMENT
UNCLASSIFIED // DISTRIBUTION A

13. SUPPLEMENTARY NOTES

14. ABSTRACT

Current high-frequency synthetic aperture sonar (SAS) imaging systems and processing software have been largely successful in producing high-quality imagery in a variety of oceanographic and seafloor environments. In most high-frequency real aperture and SAS systems, the image pixel values have been adjusted for optimal viewing by operators. The dynamic range of the pixel values may be truncated and the mean background level may vary from image to image, even across images of the same geographic area. Automated Target Recognition (ATR) algorithms that process these images require that pixel energy levels are normalized to remove systematic variations in amplitude that can cause these algorithms to fail. However, the adaptive nature of image normalization algorithms can introduce artifacts as well. In many cases the discarded original pixel values may contain valuable information. Calibrated SAS images, defined as images whose pixel values represent only the scattering properties of the seafloor or target, present a promising input to ATR because 1) they preserve amplitude information, which may provide stable feature measurements to ATR, and 2) they can be normalized without artifacts by taking into account propagation and scattering physics, potentially offering a superior method than current normalization techniques.

For this grant, measured system parameter were used to form calibrated images from a high frequency synthetic aperture sonar system. Systems with large bandwidth and wide beams cannot directly estimate the scattering cross section, since that quantity is defined using a plane wave of a single frequency for the incident field. Correspondingly, the quantities produced by calibrated images must be understood as quantities averaged over the systems bandwidth and beamwidth. Details of this method, and scattering cross section results are presented in the enclosed OCEANS2019

Analysis of Backscatter Measurements from Calibrated Synthetic Aperture Sonar Images

Peter D. Romaine
Code X11
Naval Surface Warfare Center
Panama City, US

Derek R. Olson
Oceanography Department
Naval Post Graduate School
Monterey, US

J. Tory Cobb
Senior Technologist
Naval Surface Warfare Center
Panama City, US

***Abstract*— Calibrated Synthetic Aperture Sonar (SAS) data can provide monostatic backscattering strength measurements as a function of grazing angle at high resolution. Motivated by an interest in obtaining invariant metrics from vehicle based sonar acquisition systems, an end-to-end processing methodology for recovering calibrated scattering cross section levels from seafloor swaths is presented. Calibrated SAS beamforming software developed for this work was based on the narrowband sonar equation and a delay-and-sum beamformer. Modern SAS processing techniques such as redundant phase center micronavigation, and an autofocus algorithm to estimate sound speed, were employed in the beamforming stage. Data from overlapping sections of seafloor acquired in the Gulf of Mexico during 2012 provide the basis for analysis of comparative scattering results, which are examined in an effort to demonstrate adherence to established acoustic principles.**

Keywords*— *Calibrated Synthetic Aperture Sonar (SAS), acoustic backscattering strength, grazing angle, absolute intensity

I. INTRODUCTION

High-frequency sonar imagery is commonly used for target detection and mapping purposes [1]. The dynamic range of these images is quite high and the image power depends on range due to terms in the sonar equation, such as spherical spreading, sensor directivity, attenuation, and processing gain [2]. Image analysis by human operators or machines requires a certain dynamic range to achieve good performance, so these images are typically normalized using time-varying gain (TVG). A TVG can either be based on the sonar equation [3], or empirical analysis. A simple and common empirical method of normalization is to estimate the received intensity across all channels, then divide each channel by the mean amplitude (square root of the mean power). The normalized channel data are then used to form the image using standard imaging algorithms [4], such as backprojection.

After beamforming, a secondary image pre-processing step is usually applied to the beamformed imagery to reduce the dynamic range of the pixel intensity to the appropriate bit depth of the human visual system (HVS). Typically, these approaches involved linear or non-linear compression of the tail of the low- and high-ends of the intensity distribution [5] or anchoring the scene intensity dynamic range to the statistics of the current scene [6]. These suppressions, especially when coupled with an adaptive TVG scheme as mentioned previously, distort the data and prevent estimation of quantitative acoustic metrics from the resulting image. Fig. 1 depicts an example beamformed image before Fig. 1(a) and after Fig. 1(b) applying the image normalization scheme from [6]. The seafloor and the faint target in the upper right hand corner of Fig. 1(a) are now clearly visible in Fig. 1(b) once the high-end of the dynamic range is compressed.

While these normalization schemes produce imagery pleasing to the human visual system, they distort absolute backscattering measurements from the seafloor and target. Here we seek to invert the sonar equation for synthetic aperture sonar (SAS) images to estimate backscattering strength. The scattering due to seafloor roughness and inhomogeneities is quantified by the scattering cross section per unit area per unit solid angle (heareafter called the “scattering cross section” or “cross section”). When converted to decibels, it is called scattering strength. This quantity is independent of measurement system and geometry, apart from the usual dependence of scattering strength on grazing angle, which in SAS images shows up as a range-dependent intensity. Inverting the sonar equation removes the large-scale intensity changes that are due to the measurement system, and reduces the dynamic range in a predictable way, as opposed to the empirical TVG methods described above.

Scattering strength is proportional to the mean intensity of the scattered field resulting from an interaction with a patch of seafloor [7]. The narrowband sonar equation typically used to describe scattered field behavior can be shown to apply to broadband SAS sonar systems found on unmanned underwater

This work was supported by the Office of Naval Research

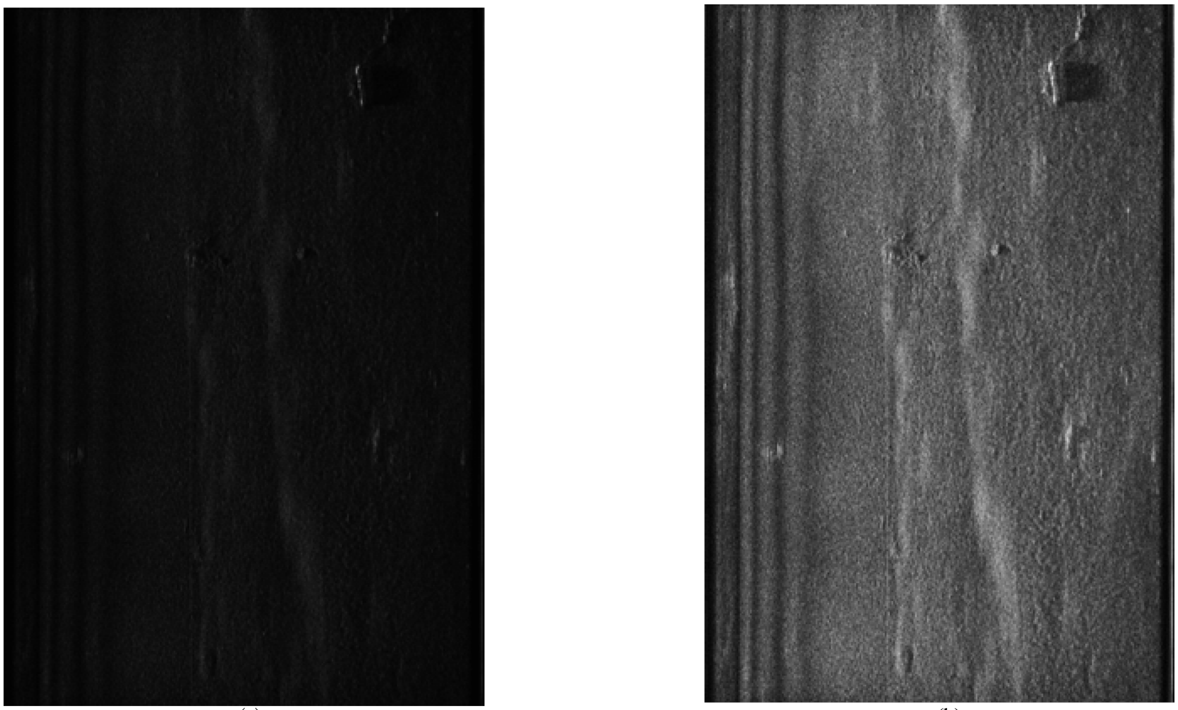

(a) (b)

Figure 1. The beamformed image before (a) and after (b) applying the image normalization scheme from (Cook 2007). The seafloor and the faint target in the upper right hand corner of (a) are now clearly visible in (b) once the high-end of the dynamic range is compressed.

vehicles (UUV). This extension is shown for the two dimensional case as outlined by work completed by Olson and Lyons [8], which concluded that the mean intensity of the scattered field can be compared across systems having varying bandwidths, so long as the center frequency is held constant. An overview of the SAS beamforming process implemented to obtain absolute scattering strength levels from the data is presented, along with the methodology for processing subsequent imagery to calculate average scattering strength as a function of grazing angle. A description of the data set provides context for discussion of the scattering strength analysis. Results are shown that compare measurements of overlapping sections of seafloor and conclusions are drawn.

II. Scattering Measurements

A. The Narrowband Sonar Equation

The scattered field measured by a sonar system depends on the imaging geometry, system parameters, and seafloor properties. When observed from a UUV platform, the transmitter and receivers are close to one another and can be considered to be a monostatic geometry. In Olson et al [9], a method to estimate the scattering cross section for each pixel in a SAS image was detailed. In that reference, the calibration method was based on system parameters that were estimated in several different ways. The element beampatterns were measured in the laboratory, but the overall source strength and receiver sensitivity was estimated by comparing data to a scattering model with known inputs. This method automatically took into account all multiplicative constants in the sonar equation, and therefore the method was able to be simplified. The method used here is based entirely on laboratory measurements of the sonar parameters, and estimates of sonar location from on-board navigation instrumentation and micronavigation [10] and requires a more rigorous accounting of all the variables. We have therefore altered the calibrated processing, resulting in the following estimate of per-pixel scattering cross section:

$$\tilde{\sigma}_i = \frac{|q_i|^2}{\Gamma_i\left(\sum_i w_{ij}\right)^2}, \tag{1}$$

$$|q_i|^2 = \sum_i^{N_r} a_{mf} \sqrt{\frac{2}{s_r s_o c\tau}\frac{cos\theta_{ij}}{\cos\left(\theta_{ij}-\theta_0\right)}\frac{1}{r_{ij}\Psi_{SE}}\frac{r_{ij}^2 e^{2\alpha r_{ij}}}{\left|b_{tx}(\theta_{ij})\, b_{rx}(\theta_{ij})\right|^2}}\, w_{ij} v_{ij}, \tag{2}$$

where $\tilde{\sigma}_i$ is the unaveraged scattering cross section of the i^{th} pixel, r_{ij} is the range from the jth sensor to the ith pixel, v_{ij} is the received voltage from the jth sensor delayed for the ith pixel, s_r is the receiver voltage sensitivity in V/Pa, s_0 is the source level in Pa×m, α is the frequency dependent absorption coefficient in radians per meter, and c is the sound velocity. The transmitted pulse length is τ, and the factor a_{mf} takes into account the gain if a matched filter is used to compress the pulse. $b_{tx}(\theta_{ij})$ is the transmitter vertical directivity pattern, and $b_{rx}(\theta_{ij})$ is that of the receiving transducer. The output of the initial stages of the beamforming process is represented by the variable q_i, for pixel i. In the beamforming stage, Eq. (2), the sonar equation has been inverted for each channel before beamforming. Eq. (1) accounts for the change in energy due to beamforming. In Eq. (2), j represents an individual sensor channel, and the subscript ij represents variables that depend on both pixel location and sensor location. The reference angle, θ_0, represents the depression angle of the main response axis and θ_{ij} the grazing angle from the j^{th} sensor channel to the i^{th} pixel. The factor Ψ_{SE} represents the angular beamwidth of a single array element, so that $r_{ij}\Psi_{SE}$ is the azimuthal dimension of the ensonified area. The parameter Γ_i takes into account both the partially coherent gain of the beamforming stage, as well as a conversion of the azimuthal resolution between a single sensor channel and a weighted linear array. The weights applied to the synthetic aperture for each pixel are specified by w_{ij}, and the coherent gain is removed from the beamformed image.

B. *Broadband Effects*

In the above analysis, the narrowband sonar equation was employed, although broadband frequency modulated pulses are commonly used in SAS systems. It is key to understand any effect of using a broadband signal on scattering strength estimates. We report result from Olson and Lyons [10], in which the Helmholtz-Kirchhoff integral equation was solved for a rough surface over a large frequency band. Time-domain signals were formed through Fourier synthesis, and Monte-Carlo estimates of scattering strengths were formed for different spatial resolutions. In Fig. 2, we plot scattering strength for a pressure-release rough surface following a one dimensional power law with a spectral strength of 〖10〗^(-5)m, and a spectral exponent of 2. The simulations used a center frequency of 100 kHz (the center frequency of the system used in Olson et al [8], which motivated [10]) and various bandwidths. From this figure, no discernable dependence on bandwidth is observed. This independence of scattering strength on pulse length for power law roughness spectra indicates that the narrowband sonar equation is appropriate. Although this simulation was performed for a one-dimensional roughness spectrum, we expect that the same relationship holds for isotropic two-dimensional roughness. Measurements in anisotropic environments may not have the same relationship, which we will note later in our analysis.

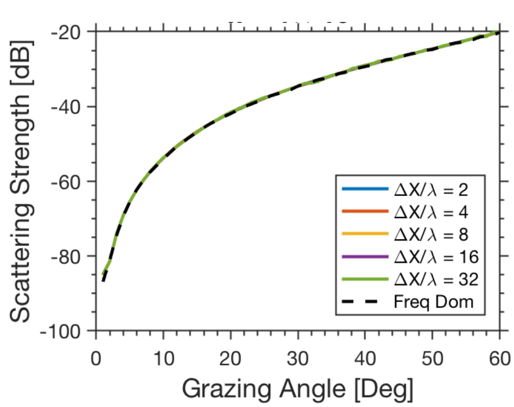

Figure 2. Result of numerical simulation of the time-domain scattering cross section estimated for different pulse spatial resolution, ΔX compared to the acoustic wavelength, λ. Results for a pure frequency domain simulation at the center frequency were also performed.

III. Data Sets and Results

A. *Overview*

The narrowband sonar equation was used to estimate $\tilde{\sigma}$ for data collected off the coast of Panama City, FL in 2012. This data set is of particular importance for our purposes because it was collected with many overlapping tracks, allowing for independent measurements over the same seafloor swaths. This collection geometry allows the comparison of scattering strength for the same patch of seafloor measured from disparate azimuthal angles. The data collection comprised lawnmower tracks in 18.8 – 19.8 m of water depth in an operation area understood to be predominantly sand. This minimal change in depth over the experimental area enables the assumption of small large-scale seafloor slope in the image. The runs processed for this analysis were of undisturbed seafloor sections and did not contain any intentionally positioned targets or objects of interest.

Several examples of calibrated images are presented in Figs. 3-5 and display backscatter strength in decibels. In Fig. 3 (a) and (b), the two images depict a similar section of seafloor having approximately 80% of overlap for the full swath. Distinguishing features of this bottom section are discernable in each image. These images were acquired from the same SAS array at vehicle headings that differed by 5°. Individual pixels from these data files were averaged in the across track (range) dimension and analyzed as a function of the corresponding grazing angle, then plotted as shown in Fig. 3 (c). These results correspond to the images (a) and (b) and show close agreement in averaged scattering levels having a mean difference of approximately 0.08 dB across applied grazing angles. Also shown in dotted line is the empirical Lambert curve, defined for the monostatic condition in equation 3.

$$\sigma = \mu \sin^2\theta_i \tag{3}$$

where μ is an empirically determined constant equal to -20 dB for this scene. This value is consistent with other values of the Lambert parameter for sandy seafloors summarized in Fig 12.3 of Jackson and Richardson [7]. Scattering strength values presented were calculated based on pixel sections depicted in the corresponding images..

B. *Analysis*

The approach outlined above was applied to the larger set of data to determine whether calibrated scattering strength is consistent for different collection geometries in the 2012 test data. This initial analysis of the calibrated processing focused on establishing repeatability of measurements taken separately but over similar sections of seafloor. The study also serves to establish a baseline from which future work can be analyzed and seeks to determine when scattering strength measurements from calibrated SAS images can be appropriately applied.

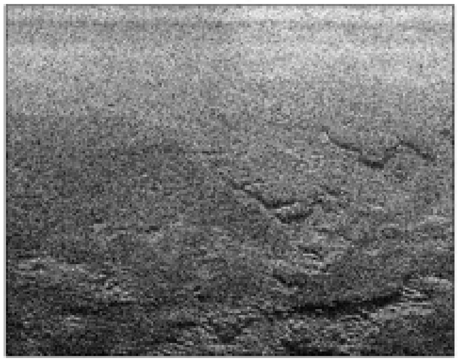

(a)

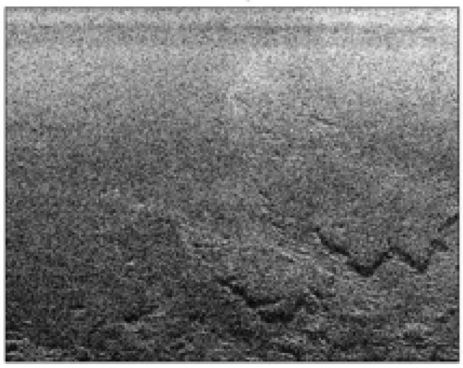

(b)

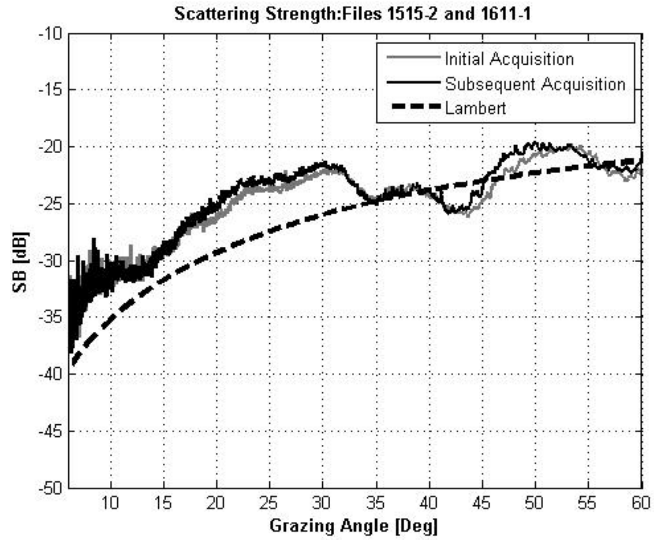

(c)

Figure 3. The calibrated image obtained during initial acquisition (a) and (b) the calibrated image processed during subsequent vehicle run. Scattering strength results from both compared to Lambert Curve (c).

Data were examined from 110 port-side images. Of these data files there were 42 instances where the images comprised seafloor sections exhibiting a nominal 60% or more of overlap. Mean difference of scattering strength in dB was compared for a relevant range of grazing angles. This was done for images acquired from similar vehicle heading, defined as within +/- 10°. Analysis was also performed for images with opposing heading, defined as vehicle heading difference > 170°.

Complete image files were trimmed in both the across track and along track axis to discard potential edge effects. Scattering strength values for each file were then averaged in the along track dimension. Grazing angles were calculated from vehicle position and image coordinates. Overall, the scattering strengths calculated via calibrated processing described above showed a 0.82 dB difference when repeat pass data was acquired under similar reflection pose and a 1.32 dB difference when acquired at opposite reflection pose, or azimuth angle. These differences represent the mean scattering strength at system relevant grazing angles and are shown in Table 1:

TABLE 1.

	Sample Size	Mean Absolute SB Difference (dB)
Same Vehicle Heading (Difference < 10°)	24	0.82
Opposite Vehicle Heading (Difference > 170°)	18	1.32

Additionally for all pose scenarios the less overlap that existed between swaths, the greater the difference in scattering measurements i.e. images having less similar sections had less similar scattering strengths, a result depicted in Table 2:

TABLE 2.

Nominal % Overlap	Mean Scattering Difference (dB)
60-69	1.21
70-79	0.91
80-89	0.63

In instances where the truncated image appeared homogeneous, calibrated scattering strengths were similar even if acquired at different azimuth angles. Fig. 4 depicts the robustness in scattering strength measurements encountered when acquisition geometries varied according to a heading difference of 180°. This result supports the acoustic understanding that a diffusely scattered field lacks directionality.

Swaths where the seafloor was discernably anisotropic (primarily directional ripples) showed large scattering strength differences. An example is shown in Fig. 5. The pockmarked bottom and rippling structure presented an interface that gave rise to an incident field highly dependent on vehicle acquisition geometry. Since the entire image was used to estimate the average scattering strength, systematic changes, such as the relative pixel fraction of the image composed of ripples,

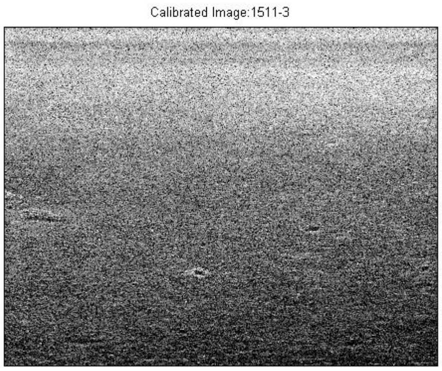

(b)

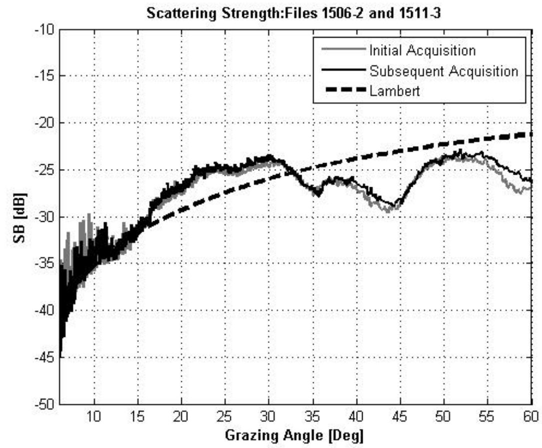

(b)

Figure 4. The calibrated image (a) and (b) scattering strength results from both compared to Lambert Curve.

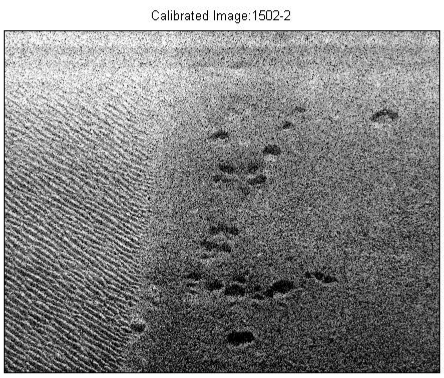

(a)

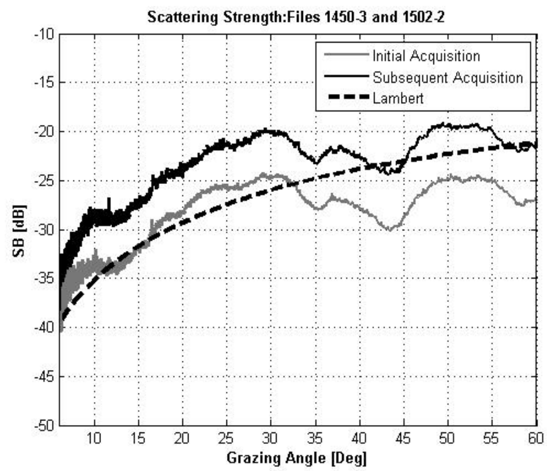

(b)

Figure 5. The calibrated image (a) and (b) scattering strength results from both compared to Lambert Curve.

pockmarks, and homogeneous sand may be responsible for the discrepancy in Fig. 5(b). Analysis using smaller image patches may reveal more consistency across imaging geometry. This is an opportunity for future research.

IV. CONCLUSION

A calibrated beamformer was developed and utilized to generate scattering strength measurements for individual pixels contained within SAS data files. The narrow band sonar equation formed the basis for this process and was shown to be extendable to broadband sonar systems through numerical simulation and the processing of sonar data from a 2012 sea test. The acquisition of multiple overlapping sections of seafloor provided an opportunity to assess the calibrated process for conformity to established acoustic principles. Analysis demonstrated that absolute scattering strengths approximated documented results for like bottom types, and review of multiple images indicated that similar seafloor sections (as defined by approximate percentage of overlap) have similar scattering strengths. Further, measured scattering strength differences are inversely proportional to percentage overlap. Anisotropic surface types presented highly variable scattering strengths when changes to vehicle geometry were introduced, whereas homogenous surface types were robust to changes in measurement when analyzed from various azimuth angles.

ACKNOWLEDGMENT

The authors would like to thank ONR Code 32 and NSWC Panama City.

REFERENCES

[1] Roy E. Hansen (2011). *Introduction to Synthetic Aperture Sonar*, Sonar Systems, Prof. Nikolai Kolev (Ed.).
[2] Urick, R. J. (1983). *Principles of Underwater Sound*, Mcgraw-Hill Book Company.
[3] G. Le. Chenadec, J.M. Boucher, X. Lurton, "Angular dependence of k-distributed sonar data", *IEEE Transactions on Geoscience and Remote Sensing*, vol. 45, pp. 1124-1235, 2007.
[4] D. Johnson "Side Scan Imagery Analysis Techniques", *OCEANS '91*, Honolulu, H1, Oct. 1991.
[5] C. Schlick, "Quantization of Techniques for Visualization of High Dynamic Range Pictures," *Photorealistic Rendering Techniques, Focus on Computer Graphics*, Springer, Berlin, pp. 7-20, 1995.
[6] D. Cook, *Synthetic Aperture Sonar Motion Estimation and Compensation*, Master's Thesis, Georgia Tech, 2007.
[7] D. Jackson and M. Richardson, *High Frequency Seafloor Acoustics*, Springer, New York, 2010.
[8] D. Olson, R., Lyons, A. P., (2018). " Broadband numerical simulation of scattering from rough pressure-release and fluid-fluid interfaces," J. Acoust. Soc. Am. 144(3).
[9] D. Olson, R., Lyons, A. P., and Sæbø, T. O. (2016). " Measurements of high-frequency acoustic scattering from glacially eroded rock outcrops," J. Acoust. Soc. Am. 139(4), 1833–1847.
[10] A. Bellettini, and M. Pinto, (2002), "Theoretical accuracy of synthetic aperture sonar micronavigation using a displaced phase-center antenna," IEEE J. Ocean. Eng. 27(4), 780-789

Resolution dependence of rough surface scattering using a power law roughness spectrum

Derek R. Olson[1, a)] and Anthony P. Lyons[2]

[1] *Oceanography Department, Naval Postgraduate School, Monterey, CA 93943*

[2] *University of New Hampshire, Durham, NH*

Contemporary high-resolution sonar systems use broadband pulses and long real or synthetic arrays to achieve high resolution for mapping and target detection tasks. The spatial resolution of these systems can approach the acoustic wavelength, and it is important to understand any affects this situation might have on quantitative measures of the scattered field, such as the scattering cross section or scintillation index. In this work, we numerically investigate the dependence of these two acoustic measures on pulse length (or equivalently bandwidth) using rough surfaces with power-law spectra. Using the boundary element method and Fourier synthesis, we found that there is no resolution dependence of the scattering cross section. We found that the scintillation index increases as resolution increases, grazing angle decreases, and spectral strength increases. This trend is confirmed for center frequencies of 100 kHz and 10 kHz, as well as for power law spectral exponents of 1.5, 2, and 2.5. The hypothesis that local tilting at the scale of the acoustic resolution is responsible for intensity fluctuations was examined. It was found that local tilting is responsible in part for the fluctuations, but other effects, such as non-local multiple scattering and shadowing likely also play a role.

[a] dolson@nps.edu

I. INTRODUCTION

Theoretical treatment of wave scattering from rough interfaces is generally performed using an incident plane wave, which by definition has a single direction and frequency, and exists over infinite spatial extent. However, experimental measurements of the scattered field typically employ broadband pulses to achieve high spatial resolution - desirable for seafloor mapping or target detection. Performance of such systems typically depends on the mean scattered intensity of the scattered field from the seafloor, and more generally its probability density function. The mean intensity is usually characterized in terms of the scattering cross σ section per unit area per unit solid angle, σ (hereafter referred to as the "cross section", "scattering cross section," or "scattering strength" for the decibel version.). Variability in the scattered intensity is often characterized using the scintillation index, SI (Ishimaru, 1978; Lyons *et al.*, 2009; Tatarski, 1961).

The scattering cross section is defined as the ratio of the scattered intensity to the incident intensity, normalized by propagation effects, as well as the energy flux of the incident acoustic wave. For some finite resolution systems at low grazing angles, this definition may be simplified to (Jackson and Richardson, 2007, p. 32),

$$\sigma = \frac{A}{r_s^2} \frac{\langle |p_s|^2 \rangle}{|p_i|^2} \tag{1}$$

where A is the ensonified area, r_s is the distance between a resolved patch of area A on the seafloor (or any rough surface, generally), p_i is the incident pressure, and p_s is the scattered pressure measured by the system. Note that this definition is valid only for geometries with well-defined incident and scattered field directions. Strictly, this definition of the scattering cross section is only true in the limit as the ensonified area becomes large compared to all length scales of interest (i.e. outer scale of the rough surface, or the acoustic wavelength), since plane waves interact with the entire rough surface. It has been demonstrated (Gauss *et al.*, 1996; Henyey *et al.*, 1995), that for finite resolution systems, the scattering strength is independent of pulse length - a consequence of Parsevals' theorem (Oppenheim *et al.*, 1999, p. 60) and linear time-invariance, and thus generally valid. However, if the properties of the ensemble of rough surfaces vary with resolution, the scattering environment has very strong frequency dependence, or is time-varying, then the measured scattering strength may depend on resolution. For high-resolution systems, it is plausible that the ensemble used to estimate the scattering cross section may change as a function of resolution, and has potential to cause a resolution dependence of the scattering cross section.

The interface scattering cross-section characterizes the mean scattered power from an interface, but a more general property of the scattered field is the probability density function (pdf) of the pressure or its complex magnitude, termed the envelope pdf. The envelope pdf is connected to performance of target detection systems, and has potential for remote sensing of the environment using high resolution systems (Lyons *et al.*, 2009, 2016; Olson *et al.*, 2019). The pressure due to scattering from a rough, homogeneous interface with Gaussian height statistics has commonly been assumed to follow a Gaussian distribution for the real and imaginary components, and a Rayleigh distribution for its complex magnitude (Jakeman, 1980)). In this situation, the scintillation index, or normalized intensity variance is unity. For heavy-tailed statistics (with more frequent large amplitude events), the scintillation index is greater than unity.

Arguments for Rayleigh distributed scattered pressure magnitude follow from the assumption of a large number of independent surface elements contributing to the scattered field (Abraham and Lyons, 2002; Jakeman, 1980). So long as the ensonfied area of a Gaussian, homogeneous rough interface is large (so there are many independent scatterers contributing to the field), this assumption holds true. Another argument for Rayleigh magnitudes follows from perturbation theory and the interpretation in terms of Bragg scattering. In this framework, the scattered pressure is proportional to the amplitude spectrum of the roughness evaluated at the Bragg wavenumber, $2k_w \cos(\theta_i)$, where k_w is the acoustic wavenumber in the water column, and θ_i is the incident grazing angle. If the surface has Gaussian statistics in the spatial domain, then the wavenumber components will have a Rayleigh distributed envelope via the central limit theorem. Since the the acoustic pressure magnitude is directly proportional to the acoustic spectrum at the Bragg wavenumber, it follows that the envelope pdf will be Rayleigh distributed as well.

Contemporary high-resolution seafloor imaging systems, such as synthetic aperture sonar (SAS) have spatial resolutions on the order of the center wavelength. Small resolution cell sizes may result in ensembles that vary with the resolved area of the seafloor, thereby causing a departure from Rayleigh statistics. The resolution dependence of SI has implications for target detection performance, synthetic aperture autofocus algorithms (e.g. (Marston and Plotnick, 2015)), and preprocessing algorithms for SAS images (Williams, 2015).

It was observed in (Lyons *et al.*, 2016) that measurements of the scintillation index from SAS images of homogeneous random rough interfaces had a strong dependence on range, which was interpreted as a result of modulation of the local slope by roughness components at the scale of the acoustic resolution or larger. This interpretation corresponds to the composite roughness model (Jackson *et al.*, 1986b; McDaniel and Gorman, 1983). Combined with interpretations in (Lyons *et al.*, 2016), this results in a dependence of the scintillation index on the acoustic resolution, the underlying pixel statistics, range (through grazing angle), as well as roughness spectrum parameters. These interpretations, while plausible, suffer from a lack of experimental confirmation.

In this paper, we examine the question of whether there is a dependence on resolution of the scattering cross section and scintillation index. Since the cross section is strictly defined for incident and scattered plane waves, a finite resolution version must be used, which is detailed below. When discussing the cross section, it is always noted whether we mean the plane wave version or finite resolution approximation. The acoustic resolution is defined as the full width half maximum spatial extent of the square of the incident pulse envelope, and is equal to $\Delta X = c/(2aB_w)$, where ΔX is the spatial resolution of the pulse[1], $1/(2aB_w)$ is the temporal resolution of the pulse in the backscattering direction, B_w is the 3dB full width bandwidth of the transmitted pulse, and c is the wave speed. The constant a depends on the shape, or point spread function of the pulse used.

These questions were investigated through numerical solution of the Helmholtz-Kirchhoff integral for the scattered pressure using the boundary element method (BEM) (Sauter and Schwab, 2011; Wu, 2000) using pressure-release boundary conditions. This method is similar to that used by (Thorsos, 1988). Fourier synthesis was used to construct the broadband scattered pressure at various spatial resolutions, and metrics were computed based on the scattered time-domain pressure. Comparisons were made to the ensemble averaged cross section performed in the frequency domain (i.e. computed at a single frequency, which is a good approximation of the plane wave case). These simulations were performed for center frequencies of both 100 kHz and 10 kHz, and for one dimensional rough surfaces with power law spectra, whose parameters are the spectral strength and spectral exponent.

Through these numerical experiments, it was found that the scattering strength does not vary as a function of bandwidth for the parameters investigated in this study. The error of this comparison is within the Monte Carlo error of this study. For scintillation index we found that it becomes greater than one as resolution increases, grazing angle decreases, and spectral strength increases. Specifically, for larger spectral exponents, the scintillation index is more sensitive to changes in spectral strength, resolution and grazing angle.

We first present an overview of the geometry and roughness statistics in Sec. II. The integral equations and discretization methods are given in Sec. III, and the incident field in Sec. IV. Methods to estimate the scattering cross section and scintillation index are given in Sec. V. We give a discussion on how the parameters of the numerical simluations were selected in Sec. VI. Results are presented in Sec. VII, with a discussion and some preliminary hypotheses given in Sec. VIII. Conclusions are given in Sec. IX

II. GEOMETRY AND ENVIRONMENT

The geometry of the scattering problem is presented in Fig. 1. The problem takes place in two dimensions with position vector $\mathbf{r} = (x, z)$. The rough interface is defined as $z = f(x)$ and is shown as the thick black line in this figure. In this figure, the nominal incident and scattered wave directions are shown with their grazing angles and nominal wave vectors.

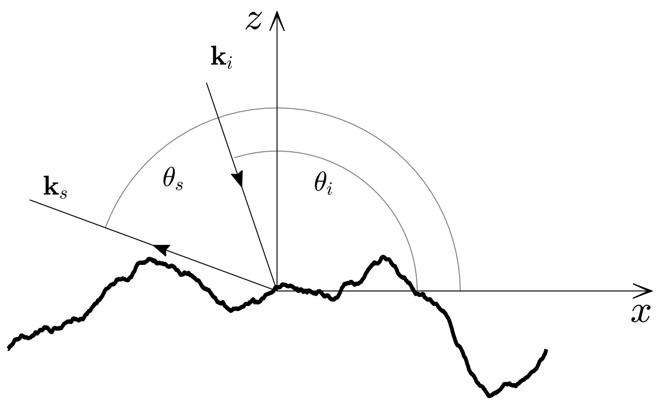

FIG. 1. caption

The sound speed in the upper medium is c, which is taken to be 1500 m/s, but our results can be applied to other sound velocities by performing the appropriate dimensional scaling. The acoustic frequency is f, and is related to the wavenumber $k = 2\pi f/c$. Simulations are performed at a center frequency f_0, and bandwidth BW. The center wavelength and wavenumber are λ_0 and k_0 respectively

The rough interface is assumed to have wide-sense homogeneity (spatial stationarity) and a Gaussian pdf. Its second order properties can be completely described by its autocovariance function,

$$B(x) = \langle f(y) f(y+x) \rangle \tag{2}$$

and power density spectrum

$$W(K) = \frac{1}{2\pi} \int B(x) e^{iKx} \, \mathrm{d}x. \tag{3}$$

Several second-order properties of this spectrum are useful for the analysis performed in this paper. In particular, the root mean square (rms) height, h^2 is given by

$$h^2 = \int_{-\infty}^{\infty} W(K)\,\mathrm{d}K = B(0). \tag{4}$$

The rms slope s^2 is

$$s^2 = \int_{-\infty}^{\infty} K^2 W(K)\,\mathrm{d}K = \left.\frac{\partial^2 B(x)}{\partial x^2}\right|_{x=0}. \tag{5}$$

The power density spectrum used in this work is the truncated power law,

$$W = \frac{w}{|K|^{\gamma}}, \tag{6}$$

for $k_l \leq |K| \leq k_u$, and zero otherwise. The spectral strength is w with units of $\mathrm{m}^{3-\gamma}$ and γ is the dimensionless spectral exponent. The lower wavenumber cutoff is $k_l = 2\pi/L$, where L is the outer scale. The upper wavenumber cutoff is $k_u = 2\pi/\ell$, where ℓ is the inner scale. Random realizations are produced from this power spectrum using the Fourier synthesis technique detailed in (Thorsos, 1988). Since $f(x)$ is a real function, both positive and negative wavenumbers are included in the Fourier integral. We identify the outer scale with the length of the rough surface, and the inner scale with the sampling interval of the rough surface realization.

For the power-law form used here, the non-dimensional mean square slope and mean square height are

$$s^2 = \frac{2k_0^{3-\gamma} w}{3-\gamma}\left[\left(\frac{k_u}{k_0}\right)^{3-\gamma} - \left(\frac{k_l}{k_0}\right)^{3-\gamma}\right] \tag{7}$$

$$k_0^2 h^2 = \frac{2k_0^{3-\gamma} w}{\gamma-1}\left(\frac{k_0^{\gamma-1}}{k_l^{\gamma-1}} - \frac{k_0^{\gamma-1}}{k_u^{\gamma-1}}\right). \tag{8}$$

These parameters have been expressed in a form where the terms outside and inside the parentheses are dimensionless. Although the upper wavenumber is set by the discretization interval, δx, the way in which the rough surfaces enter into the acoustical simulations may be subject to an effective upper limit, $k_{ueff} = 2\pi/\ell_{eff}$, where ℓ_{eff} is an effective inner scale. Roughness components with wavenumbers much greater than k likely have an insignificant effect on the scattered field, making the effective upper limit much less than that defined by the surface sampling. RMS height is insensitive to the upper cutoff, and more sensitive to the low-wavenumber cutoff. RMS slope is sensitive to the upper cutoff, and insensitive to the lower cutoff, so long as it is sufficiently small. To make the upper limit explicit, we will use the notation s_ℓ to denote the rms slope computed using $k_u = 2\pi/\ell$ for some length scale ℓ.

III. INTEGRAL EQUATIONS AND DISCRETIZATION

We perform this study numerically using a discretized form of the 2D Helmholtz-Kirchhoff integral equation for Dirichlet boundary conditions (Thorsos, 1988). Although our motivation for this work is seafloor scattering, the assumption of a Dirichlet boundary allows us to focus solely on the role of the rough interface. For a single frequency, this integral equation is

$$p\left(\mathbf{r}_p\right) C_p = p_i\left(\mathbf{r}_p\right) + \int\limits_S \frac{\partial p\left(\mathbf{r}_s\right)}{\partial n_s} G_k\left(\left|\mathbf{r}_s - \mathbf{r}_p\right|\right) \mathrm{d}S, \tag{9}$$

where C_p is 1/2 on the rough interface, unity in the fluid medium above the rough interface, and zero below the interface. p_i is the incident pressure, p is the total pressure, and $\partial p/\partial n$

is the total pressure normal derivative. $\mathbf{r}_p = (x_p, z_p)$ is a point in space, $\mathbf{r}_s = (x_s, z_s)$ is a point on the rough surface, and $G_k(R) = (i/4)H_0^{(2)}(kR)$ is the 2D free-space Green function (Devaney, 2012, p. 6), where $H_0^{(2)}(z)$ is the zeroth-order Hankel function of the second kind. Note that this integral equation can also describe electromagnetic scattering from 1D corrugated surface with perfectly conducting boundary conditions subject to an incident wave with TM (p) polarization (Toporkov *et al.*, 1998).

The scattering problem is solved in two steps. First, the point $\mathbf{r}_p$ is taken to the boundary. Application of the boundary conditions results in the equation

$$-\int_S \frac{\partial p\left(\mathbf{r}_s\right)}{\partial n_s} G_k\left(\left|\mathbf{r}_s - \mathbf{r}_p\right|\right) \mathrm{d}S = p_i\left(\mathbf{r}_p\right) \tag{10}$$

This equation is numerically solved for $\partial p/\partial n$ on the surface. Once this quantity is known, Eq. (9) is then evaluated with $\mathbf{r}_p$ in the far field.

Numerical solution of Eq. (10) is performed by discretization of the integral equation using boundary element method (Sauter and Schwab, 2011; Wu, 2000). In particular, we use piecewise linear basis functions to approximate $\partial p/\partial n$, and collocation to compare the true and approximate solution at discrete points. These two methods convert the integral equation into a linear system,

$$Vy = b, \tag{11}$$

where y is the solution vector consisting of the basis function coefficients used in the approximation for $\partial p/\partial n$, and $b = p_i$ evaluated at the discrete collocation points $\mathbf{r}_m = (x_m, z_m)$. The matrix V has elements

$$V_{mn} = -\int G_k\left(\left|\mathbf{r}_m - \mathbf{r}_s\right|\right) \phi(\xi_n(\mathbf{r}_s)\mathrm{d}S \tag{12}$$

Here, $\phi(\eta)$ is a linear basis function defined on the interval $\eta \in [-1, 1]$ - a symmetric triangular function centered at zero with a maximum of 1. Outside of the interval, ϕ is zero. The function ξ_n maps the basis function centered at the n-th point from physical space, $\mathbf{r}_s$ to the η domain. In this case, the basis functions are centered at the same collocation points $\mathbf{r}_m$, resulting in a square matrix. Integration is carried out using Gauss-Legendre quadrature (Abramowitz and Stegun, 1972). Due to the weak singularity in the Green's function, the diagonal elements of the matrix are computed using a sixteen point quadrature rule combined with a variable transformation whose Jacobian exactly cancels the singularity (Wu, 2000). Nonsingular matrix elements were computed using an eight point quadrature rule. LAPACK routines were used to solve the linear system using LU decomposition and back substitution (Anderson *et al.*, 1999).

Collocation points are defined on the rough surface, (x_m, z_m) with equal spacing, δx on the horizontal axis. From these points, a cubic spline approximation is used to construct a continuous and smooth surface. This interpolation forces the surface normal, and thus $\partial p/\partial n$ to be continuous, which improves the convergence rate of the discretization of the integral operator (Atkinson, 1997).

Once the surface pressure normal derivative is found, it is propagated to the field using Eq. (9) with $\mathbf{r}_p$ in the far field. In this work, the field points are equally spaced intervals of one degree at radius R. The far field radius is defined to be about 25 times the Rayleigh distance from the surface, d^2/λ_0. This criterion for the far-field is quite conservative (Jackson and Richardson, 2007, Appendix J), (Lysanov, 1973; Winebrenner and Ishimaru, 1986), although it enables the use of asymptotic expansions for the Hankel function.

IV. INCIDENT FIELD

The incident fields used in this work are broadband pulses whose spatial dependence is an approximation of a plane wave. The nominal direction of the incident wave vector are specified as vectors in Fig. 1. Their lengths vary due to the broadband nature of the field, although the center wave vectors can be defined at the center frequency by the expressions $\mathbf{k}_{0i} = (k_{0ix}, k_{0iz})$ and $\mathbf{k}_{0s} = (k_{0sx}, k_{0sz})$. The components are defined in terms of the grazing angles θ_i and θ_s (with respect to the horizontal axis) by

$$k_{0ix} = -k_0 \cos\theta_i \qquad k_{0sx} = k_0 \cos\theta_s \tag{13}$$

$$k_{0iz} = -k_0 \sin\theta_i \qquad k_{0sz} = k_0 \sin\theta_s \tag{14}$$

The center wavenumber k_0 is defined by an average of the wavenumber weighted by power spectrum of the transmitted source

$$k_0 = \int_{-\infty}^{\infty} k S^2(f)\,\mathrm{d}f, \tag{15}$$

where $S(f) = \int s(t)\exp(-i2\pi f t)\,\mathrm{d}t$ is the linear (amplitude) spectrum of the transmitted pulse, $s(t)$. The transmitted pulse used here was a complex exponential multiplied by a Gaussian envelope, with the form $s(t) = p_0 \exp\left(-t^2/\tau^2 + i\omega_0 t\right)$, where τ is a parameter of the pulse length, and ω_0 is the center angular frequency, related to the center frequency, f_0 by $f_0 = \omega_0/(2\pi)$. The factor p_0 is the pressure at the center of the pulse envelope and is included to make the dimensions consistent, taken to be 1 Pa in this work.

The temporal resolution of the pulse, $\Delta\tau$ is defined by the duration of the pulse envelope between its half power points. For the Gaussian pulse used, this quantity can be obtained by solving the equation $\exp\left(-(\Delta\tau/2)^2/\tau^2\right) = 1/\sqrt{2}$, resulting in $\Delta\tau = \tau\sqrt{2\ln 2}$. This definition of the temporal resolution results in a full width half power bandwidth of $BW\Delta\tau = 2\ln(2)/\pi \approx 0.44$. For reference, if a rectangular function with full width of BW is used for $S(f)$, then $BW\Delta\tau \approx 0.88$. The same relationship is obtained if constant envelope pulse of length $\Delta\tau$ is used. Although the rectangular pulse has a larger time-bandwidth product, the Gaussian pulse has no appreciable sidelobes in the time-domain, but requires a computational bandwidth much larger than BW to approximate a true Gaussian function.

Broadband fields are synthesized from single frequency approximations of a plane wave. This narrowband field is the extended Gaussian beam developed in (Thorsos, 1988) that provides tapering to guard against edge effects entering into the scattering calculation. The form of this field (adapted to our time convention) is given by

$$p(\mathbf{r}) = \exp\left(-i\mathbf{k}_i \cdot \mathbf{r}\left(1 + w(\mathbf{r})\right) - \left(x - z\cot\theta_i\right)^2\right), \tag{16}$$

where

$$w(\mathbf{r}) = \left(kg\sin\theta_i\right)^{-2}\left[2\left(x - z\cot\theta_i\right)^2/g^2 - 1\right], \tag{17}$$

and g is a width parameter of the incident field. For broadband simulations, Eq. (16) is used for each frequency. Since the Gaussian function has an infinite domain of support, it must be truncated to use in numerical simulations.

The function $w(\mathbf{r})$ improves the agreement between the numerical solution of the Helmholtz-Kirchhoff integral equation and its normal derivative. Discrepancies between these two solutions can result because the incident field satisfies the Helmholtz equation approximately to order $(kg\sin\theta_i)^2$ (Thorsos, 1988). Good agreement between the two solutions was observed when $kg\sin\theta_i$ is large. Therefore, to analyze low-grazing angles, (which are important to contemporary synthetic aperture sonar systems, e.g. (Bellettini and Pinto, 2009; Dillon, 2018; Fossum *et al.*, 2008; Pinto; Sternlicht *et al.*, 2016)), the parameter g must grow as θ_i approaches zero. This requirement can be thought of as enforcing the contraint that the angular width of the incident beam (full width half max),

$$\Delta\theta = \frac{2\sqrt{2\log(2)}}{kg\sin\theta_i} \tag{18}$$

should be small compared to θ_i. When the relative angular width, defined as $\Delta\theta/\theta_i$ is not small, the direction of the incident field is spread over a large range of angles, and is thus not well defined.

V. ESTIMATING TIME-DOMAIN QUANTITIES OF THE SCATTERED FIELD

The time-domain pressure is computed by

$$p(t,\theta_i,\theta_s) = \int_{-\infty}^{\infty} S(f)p(f,\theta_s,\theta_i)e^{i(2\pi f/c)R+i2\pi ft}\,\mathrm{d}f \tag{19}$$

where $p(f,\theta_s,\theta_i)$ is the scattered pressure measured at θ_s with an incident field having frequency f, and incident grazing angle θ_i. The first term in the exponential removes the time delay associated with propagation to the far field, so that the $p(t)$ can be mapped to the rough interface. The scattered grazing angle, θ_s is computed using the location at which the pressure is calculated in the far field, $\theta_s = \tan^{-1}(z_s/x_s)$. In practice this integral is computed using the fast Fourier transform (FFT).

An example realization of the scattered pressure the frequency domain is plotted in Fig. 2(a). The frequency domain pressure is plotted as the raw scattered pressure, and also weighted by the amplitude spectrum. The time-domain pressure squared after weighting by $S(f)$ and an inverse Fourier transform, is plotted in Fig. 2(b). It contains fluctuations on the time-scale of the pulse length, as well as deterministic changes due to the incident beam used in the Helmholtz integral calculations. The deterministic component must be removed before estimating the scattering cross section. This can be performed by dividing the pressure magnitude squared by the energy flux density, and multiplying it by $2\rho c/\sin\theta_i$. This quantity is equal to

$$\begin{aligned} e_f(x) = &\exp\left(-2x^2/g^2\right) \times \\ &\left(1 + \frac{2x\cot\theta}{ikg^2} + \frac{4x^2\cot^2\theta_i\csc^2\theta_i}{g^2k^2} + \right. \\ &\left. +(2x^2/g^2 - 1)\frac{\csc^2\theta_i}{g^2k^2}\right) \end{aligned} \tag{20}$$

If $kg\sin\theta_i >> 1$, then this expression can be approximated with $\exp(-2x^2/g^2)$. However, the full version of Eq. (20) is used in all cases here. The position argument, x is the position corresponding to time t in the scattered pressure. It is a function of the incident grazing angle and is defined as $x(t,\theta_i) = -ct/(2\cos\theta_i)$. The negative sign is a consequence of the definition of the angles in Fig. 1. This coordinate change is used later to map the scattered time series to locations on the rough surface.

To remove effects of the pulse length and cylindrical spreading, the squared magnitude is multiplied by r and divided by $c\Delta\tau/(2\cos\theta_i)$. To summarize, the dimensionless scaled intensity is defined as

$$q(t)^2 = \frac{r|p(t)|^2}{e_f(x(t,\theta_i))}\frac{2\cos(\theta_i)}{c\Delta\tau} \tag{21}$$

This quantity is plotted in Fig. 2 for size different pulse resolutions.

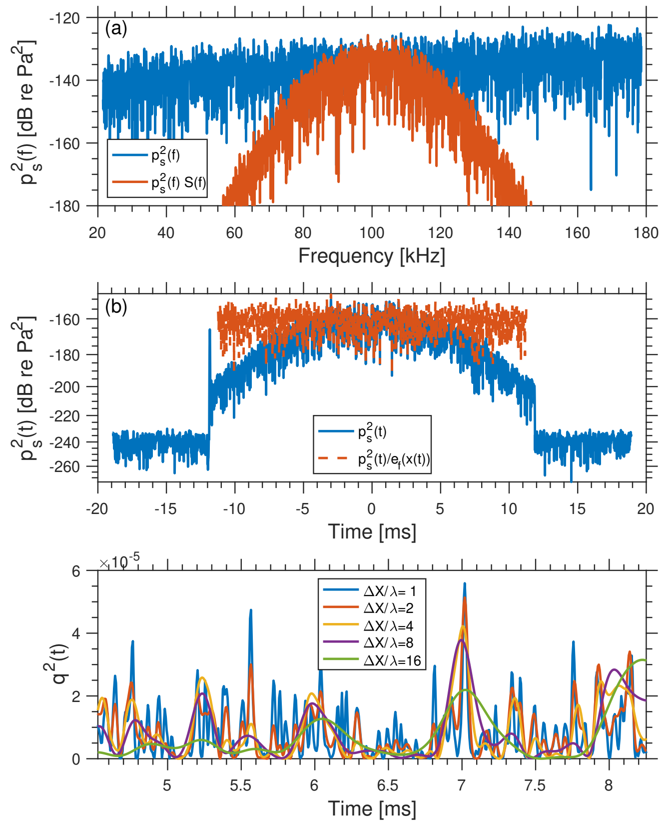

FIG. 2. (color online) Steps to estimate scattering cross section.

The scattering cross-section can be estimated by a simple average of q^2,

$$\sigma = \langle q^2 \rangle_{t,N_e}. \tag{22}$$

This ensemble average is over time, t as well as N_e, the number of rough surface realizations. Averaging over time was performed after $q(t)$ was decimated to obtain statistically independent samples, following (Abraham and Lyons, 2004). Averaging over the roughness ensembles is performed to reduce uncertainty in the σ or SI estimate and is achieved by concatenating the time series obtained from each realization and averaging the resulting vector. In practice, only 95% of the time series from the rough surface is used in the ensemble average, to ensure that edge effects do not contaminate the time series (see the spike at -12 ms in Fig. 2(b)). An example of $q^2(t)$ is plotted in Fig. 2(c) for different resolutions.

We also examine the scintillation index, SI, which is the variance of the scaled intensity, $I = q^2$ divided by the square of the mean intensity (Ishimaru, 1978, p. 437),

$$SI = \frac{\langle I^2 \rangle - \langle I \rangle^2}{\langle I \rangle^2}. \tag{23}$$

The scintillation index characterizes the fluctuations in the scattered field. If $SI = 1$, then the magnitude of the complex pressure (known as the envelope) has a Rayleigh distribution and its real and imaginary components are Gaussian. If $SI > 1$, then the pdf of the scattered field is heavy-tailed, which means that there is a higher probability of occurrence of high amplitude events compared to the Rayleigh distribution.

VI. PARAMETERS OF NUMERICAL EXPERIMENTS

A. Signal Parameters

The objective of this work is to study the resolution (or bandwidth) dependence of the scattered field. Our experiments covered the resolutions typically used in narrowband scattering experiments (Jackson *et al.*, 1986a; Williams *et al.*, 2002; Williams and Jackson, 1998), with the resolution cell on the order of 10 or more wavelengths, down to a value of one wavelength, which is on the order of what is achievable by modern SAS systems. We used specific values of $\Delta X/\lambda = (1, 2, 4, 8, 16)$. The proportional spatial resolutions correspond to temporal resolutions $\Delta\tau f_0 = (2, 4, 8, 16, 32)$ at small grazing angles, since $\Delta X = \Delta\tau/(2\cos\theta_i)$ for backscattering.

High frequency acoustic imaging systems provided the motivation for this work, and thus the simulations used a center frequency of 100 kHz. However, the parameters of the simulation were specified in a non-dimensional fashion. As long as every dimensional quantity is scaled properly, results of these simulations should be valid for lower frequencies with larger roughness parameters. To check whether the non-dimensional scaling was valid, we performed one of the simulations at 10 kHz as well, and scaled the roughness parameters accordingly. A sound speed of 1500 m/s was used for all simulations.

B. Roughness parameters

Roughness parameters were specified using only two dimensional constants, wavenumber, k (through a combination of f_0 and c) and spectral strength, w. Three spectral exponents were used, $\gamma = 1.5, 2, 2.5$, since this parameter has been observed to vary for measured seafloor roughness (Jackson and Richardson, 2007, Ch 6). Only cases of $\gamma = 2$ were performed for both 100 kHz and 10 kHz. The $\gamma = 1.5$ and $\gamma = 2.5$ simulations used a center frequency of 100 kHz only.

It now remains to specify the spectral strength. For $\gamma = 2$, we used spectral strengths of $w_{\gamma=2} = (1\times10^{-6}, 1\times10^{-5}, 2\times10^{-5}, 3\times10^{-5}, 4\times10^{-5})$m, where we have used a subscript on the spectral strength to denote that it is used for a specific value of the spectral exponent. These values resulted in $SI \approx 1$ for the smallest w, and $SI > 1$ for larger values. These values span the smaller end of the roughness measurements with spectral exponent ≈ 2 summarized in Table 6.1 of (Jackson and Richardson, 2007).

It was desired that the simulation parameters were set such that they resulted in similar values of SI for different spectral exponents. Based on interpretation that roughness at horizontal scales larger than the resolution cause changes in the local slope of the seafloor, we set the spectral strengths for $\gamma \neq 2$, such that the rms slope (Eq. (7)) was equal across different γ. Since pulses with a finite spatial resolution were used, it seems reasonable that an effective upper limit k_{ueff} is imposed on the rough surface based on the spatial resolution. With this requirement, w for other γ (denoted by w_γ), were computed using

$$w_\gamma = w_{\gamma=2}(3-\gamma)\frac{k_{ueff} - k_l}{k_{ueff}^{3-\gamma} - k_l^{3-\gamma}} \tag{24}$$

where k_l is the lower limit of the wavenumber spectrum, and k_{ueff} is the effective upper wavenumber limit. We set $k_{ueff} = 0.5k_0$ based on the values of $\Delta X/\lambda$ studied here.

Roughness parameters for the 100 kHz simulations are summarized in Table I. For the 10 kHz simulations, we chose to keep the same s^2 and kh. This condition can be satisfied if the spectral strength, surface length, and sampling interval for 100 kHz and $\gamma = 2$ are all multiplied by 10.

C. Sampling parameters

The sampling interval, δx was specified to minimize the discretization error of the integral equation. Since very large numbers of independent samples were used, our estimates of the scattering cross section had uncertainty of about 0.2-0.3 dB. It was found that an observable bias with this uncertainty in the scattering strength occurred if $\delta x/\lambda_0 > 12$, which is due to

γ	w	$s^2_{\delta x}$	$s^2_{\Delta X}$	$s^2_{2\Delta X}$	$s^2_{4\Delta X}$	$s^2_{8\Delta X}$	$s^2_{16\Delta X}$	$k_0 h$
-	$\mathrm{m}^{3-\gamma}$	$\circ$	$\circ$	$\circ$	$\circ$	$\circ$	$\circ$	-
	1.00e-06	6.40	1.66	1.17	0.83	0.58	0.41	0.95
	1.00e-05	19.52	5.23	3.70	2.62	1.85	1.30	2.99
2	2.00e-05	26.63	7.37	5.22	3.70	2.61	1.84	4.23
	3.00e-05	31.55	9.00	6.39	4.52	3.20	2.25	5.18
	4.00e-05	35.34	10.37	7.37	5.22	3.69	2.60	5.98
	1.02e-07	14.58	1.95	1.16	0.69	0.41	0.24	0.34
	1.02e-06	39.44	6.16	3.67	2.18	1.30	0.77	1.06
1.5	2.04e-06	49.31	8.68	5.18	3.09	1.84	1.09	1.51
	3.06e-06	54.93	10.59	6.34	3.78	2.25	1.34	1.84

discretization error. A conservative value of $\delta x/\lambda_0 = 15$ was therefore used to minimize this bias.

Our focus in this work is moderate to low grazing angles. The lower limit to the grazing angles that can be reliably estimated is set by the surface length, which in turn is set by the memory limitations and acceptable number of CPU hours used. These latter constraints limited us to $g = 250\lambda$. At the center frequency, the relative angular width for that value of g was about 3.5% at 10° grazing angle. Lower frequencies are more of a problem, since for a constant value of g, decreasing the frequency will increase the angular width of the field. At the lower 6 dB down point of the largest bandwidth signal used (equivalent to $0.844 f_0$), the angular width for $g = 250\lambda$ was approximately 4.2° at a nominal angle of 10° grazing angle. With these angular widths, 10° was taken to be an acceptable, if conservative, lower limit to the grazing angles that can be reliably estimated in this work. Lower angles result in a larger relative angular width which increases quadratically with θ_i. In choosing the surface length, we increased g to 400λ and did not observe any change in the behavior of σ or SI above 10°. Grazing angles less than 10° likely require fast approximate methods to solve the integral equation, such as the fass multipole method (Liu, 2009), or heirarchical matrices (Hackbusch, 2015).

The total rough surface length, L was set to $4.5g$ to allow the incident field taper to decay sufficiently at the edges of the computational domain. For the proportional bandwidths studied in this work, these surface parameters resulted in surfaces with $N = 16,875$ points. The matrix V resulting from this discretization required 4.3 GB of memory storage for double precision complex numbers.

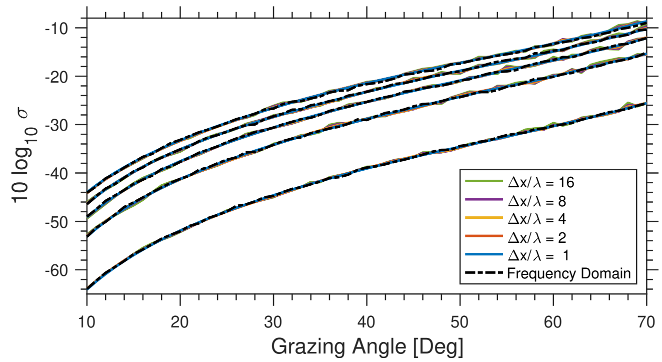

FIG. 3. Scattering Strength comparison. 100 kHz, $\gamma = 2$

The frequencies required for the largest bandwidth simulation $\Delta\tau f_0 = 2$, spanned approximately 0.2 f_0 to 1.8 f_0. This computational bandwidth was about seven times the largest 3dB bandwidth used for the Gaussian spectrum. Using a frequency spacing of $\delta f = c/(3L)$, the number of frequencies per simulation was approximately 6000. Simulations were performed on the Hamming high performance computing cluster at the Naval Postgraduate School.

VII. RESULTS

We present results for backscattering strength as a function of grazing angle, θ_i, resolution ΔX, and spectral strength, w, in Fig. 3 for $f_0 = 100$ kHz and $\gamma = 2$. Finite resolution scattering strength as well as the frequency domain version is plotted on the vertical axis, with grazing angle on the horizontal axis. Each resolution is plotted as a different color, with the frequency domain version as a black dashed-dot line. Results for different spectral strengths are on the same figure since they are well separated from one another, with the smallest w corresponding to the lowest scattering strength.

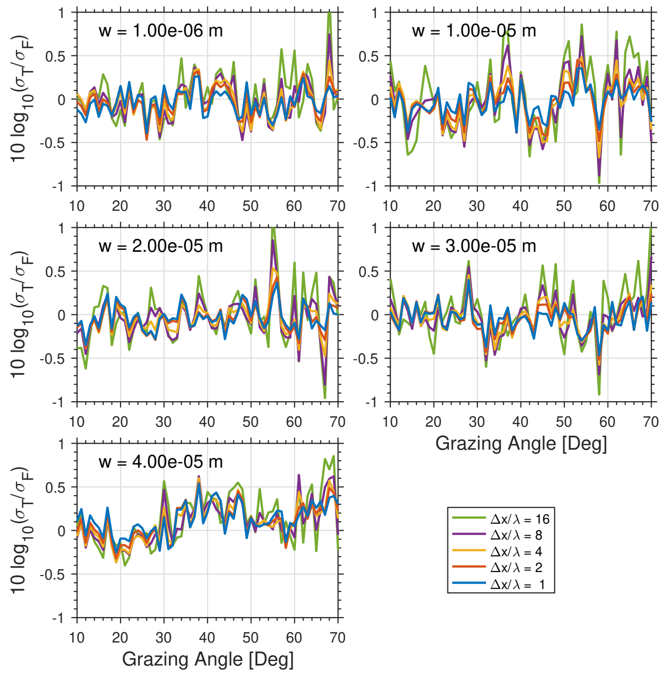

FIG. 4. Scattering Strength ratio. 100 kHz, $\gamma = 2$

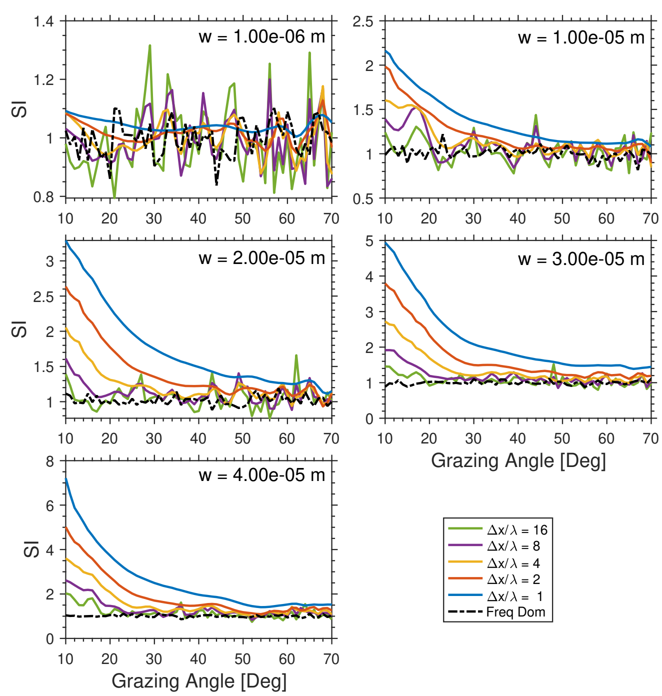

FIG. 5. Scintillation Index. 100 kHz $\gamma = 2$

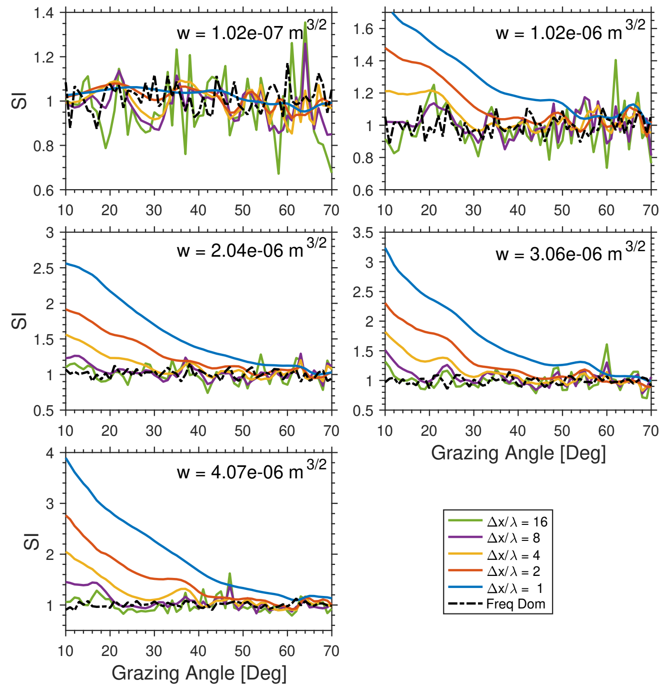

FIG. 6. Scintillation Index 100 kHz, $\gamma = 1.5$

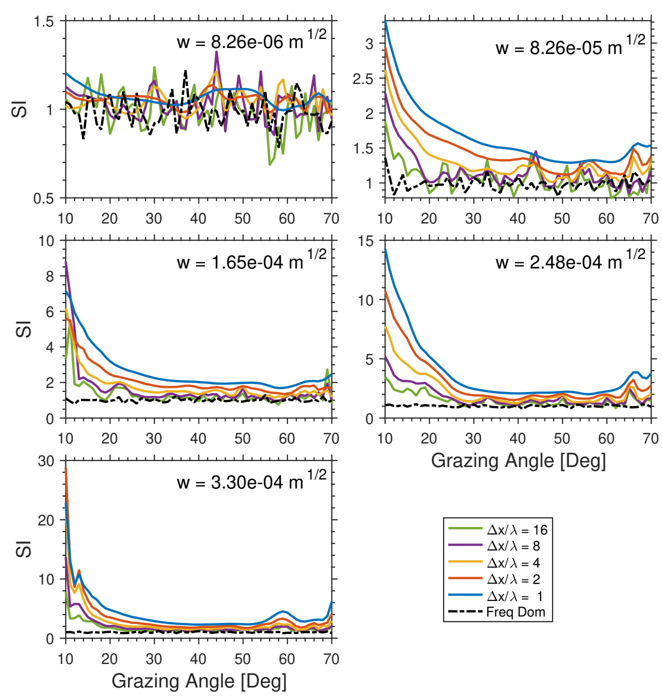

FIG. 7. Scintillation index 100 kHz, $\gamma = 2.5$

The angles are limited to a lower limit of 10° grazing angle due to finite surface length, and an upper limit of 70°, due to the difficulty in estimating the cross section near vertical using broadband pulses (Hefner, 2015; Hellequin *et al.*, 2003). To compare these results more closely, the broadband cross section is divided by the frequency-domain cross section and the dB value taken. This quantity, which we call the dB error, is plotted in Fig. 4. For all cases in these figures, there is insignificant difference between the apparent cross section in the time domain, and the frequency-domain cross sections for most w. At the largest spectral strength, some systematic oscillations as a function of θ_i are present, but cannot be easily disentangled from the rapid Monte-Carlo fluctuations. Other than that case, all differences appear to be random and within the uncertainty of the Monte-Carlo simulations. This is the expected result using Parseval's theorem, discussed in (Gauss *et al.*, 1996; Henyey *et al.*, 1995), and confirms that broadband signals can successfully be used to estimate scattering strength from a power-law seafloor with spectral exponent $\gamma = 2$.

The scintillation index for this case is plotted in Fig. 5 for broadband signals as well as the single frequency case. Each spectral strength is plotted in its own subfigure, and each resolution has its own line within the subfigure. The vertical axis is SI, and the horizontal axis is grazing angle in degrees. The narrowband result is approximately unity for the entire angular domain shown, for all spectral strengths. This is the expected result if the central-limit theorem is employed, or if the scattered field is well-described in terms of Bragg scattering. For the broadband signals, there is a profound dependence on resolution, with the scintillation index increasing as the resolution cell becomes small. This behavior can be seen in the example realization shown in Fig. 2(c). As ΔX becomes small, the intensity peaks become higher, even though q^2 is normalized by the ensonified length of the interface. Additionally, holding resolution constant, the scintillation index increases as the grazing angle becomes small, monotonically for this case. For most broadband cases, SI asymptotically approaches unity as grazing increases to its upper limit.

However, for the highest resolution cases, $\Delta X/\lambda = \{1, 2\}$, and the largest spectral strengths, this high angle asymptote is greater than one, indicating that for all angles examined here, scattered complex pressure magnitude is non-Rayleigh. In (Lyons *et al.*, 2016) a K distribution was required to describe the pdf of the scattered field at moderate grazing angles, which agrees with this result. The Monte-Carlo fluctuations are significantly less than the difference between the high-angle SI asymptote and unity, indicating that this is a statistically significant finding. We also note that (Lupien, 1999) has observed non-Rayleigh scattering for broadband scattering from rough surfaces with a power-law exponent of $\gamma = 3$, but statistical tests barely rejected the Rayleigh distribution. That analysis did not remove the effect of the Gaussian taper, so the conclusions are not comparable to the present work.

Narrowband and broadband scattering scattering strength and scintillation index were also computed for 10 kHz, $\gamma = 2$, and spectral strengths that were ten times the value in the previous section. The relative resolution, $\Delta X/\lambda$ was held constant, but consequently the resolution ΔX was a factor of 10 larger. These parameters were chosen such that the dimensionless second-order quantities were the same as in the previous 100 kHz simulations. It was found that the scattering strengths, scattering strength dB error, and the scintillation index were the same for the 10 kHz and 100 kHz cases, to within Monte-Carlo fluctuation. This set of simulations was performed to verify that characterizing the simulations nondimensionally was valid. Since plots for the 10 kHz case do not add significantly new information, they are not shown here. These results indicate that departure from Rayleigh statistics is not isolated to high-frequency imaging systems, and may occur in in lower-frequency sonar systems as well, so long as the seafloor has the appropriate roughness parameters.

The spectral exponent was changed to $\gamma = 1.5$ to examine the effect of changing the shape of the power spectrum. New values of w were used, specified in Table I. Again, the scattering strength is the same whether computed at the center frequency, or using broadband pulses in the time domain. Scattering strength comparisons and the dB error are not shown. The scintillation index is plotted in Fig. 6, and it depends on angle, resolution, and spectral strength, as in the previous two cases. The SI curves were expected to behave similarly for $\gamma = 2$ and $\gamma = 1.5$ at $\Delta x/\lambda = 2$. While SI depends on resolution in a similar fashion, it is less than the SI for $\gamma = 2$, and is less sensitive to resolution, spectral strength, and grazing angle.

Finally, the spectral exponent was changed to $\gamma = 2.5$. The values of spectral strength can be found in Table I. Again, the scattering cross section computed at the center frequency and using broadband pulses were the same to within the Monte-Carlo error of the simulations, and are not shown here. The scintillation index is plotted in Fig. 7, and again depends on resolution, spectral strength and grazing angle. As the spectral strength is increased in the same proportions as the earlier plots (the second through fifth spectral strengths are 10, 20, 30, and 40 times the smallest spectral strength respectively), the scintillation index increases much more rapidly than either the $\gamma = 2$ and $\gamma = 1.5$ cases. For large values of spectral strength, the SI has some peaks near $60°$.

VIII. DISCUSSION

In the results presented above, we have shown that scattering strength when estimated using broadband pulses is indistinguishable from its narrow-band quantity, and is independent of pulse length. This conclusion is not surprising, given the requirements of Parseval's theorem. However, as the pulse length changes, the properties of the ensemble used to estimate scattering strength changes as well. It is encouraging to see that although the ensemble is changing with respect to resolution (i.e the rough patch within a resolution cell is different for each resolution), σ is invariant to pulse length. We expect this result to hold for 3D environments as well if the roughness is isotropic. High-resolution systems are able to reliably estimate scattering strength, and it may be a stable feature for use in seabed classification. However, for highly anisotropic, non-stationary scenarios, such as those studied by (Lyons *et al.*, 2010; Olson *et al.*, 2019, 2016), the measured scattering strength may depend on pulse length.

We have also shown that the scintillation index (also called structure (Wang and Bovik, 2002; Wang *et al.*, 2004), lacunarity (Williams, 2015), or contrast (Marston and Plotnick, 2015)) is highly dependent on all the parameters studied: resolution, grazing angle, spectral strength, and spectral exponent. For moderate to low grazing angles, SI monotonically increases as grazing angle decreases, resolution cell decreases, and spectral strength increases. SI is larger for larger γ. Contrary to scattering strength, SI, and therefore the scattering process in general, is fundamentally different in the frequency and time domains for broadband pulses.

In (Lyons *et al.*, 2016), it was hypothesized that the physical cause of heavy-tailed statistics in high resolution sonar imagery was local tilting of the seafloor due to roughness wavelengths larger than the acoustic resolution. The scattered amplitude (envelope) was modeled as a product between a Rayleigh-distributed random variable (due to sub-resolution roughness), and a random variable that took into account the scattering cross section of the small scale roughness, evaluated at the nominal grazing angle modified by the local slope. Through the composite roughness approximation, local tilting (due to large-wavelength roughness components) modulates the Rayleigh-distributed field and causes the intensity variance to be greater than that of the Rayleigh distribution (i.e greater than unity). An rms slope with an upper cutoff of $2\pi/\Delta X$ was used as the input parameter to the composite roughness model, which was then used to compute the scintillation index. Given this interpretation, SI increases monotonically with rms slope, holding grazing angle constant.

A broad test of this hypothesis can be performed if we examine the resolution dependence of SI at a single angle and single spectral strength, but vary the spectral exponent. If γ is large, then the roughness will have less energy at high wavenumbers, and more if γ is small. If ΔX is decreased by, eg. a factor of two, then the effective rms slope will change as a function of γ. For γ of 1.5, 2 and 2.5 respectively, the effective rms slope will increase by a factor of 1.68, 1.41, and 1.19 respectively. Based on this interpretation, we would expect SI to be most sensitive to resolution for small γ

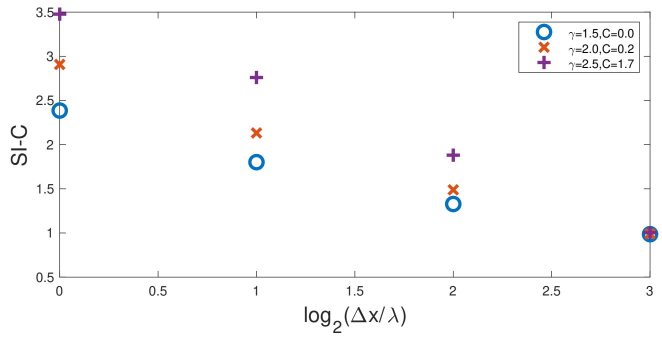

FIG. 8. SI for three different value of γ. A constant has been subtracted from SI for $\gamma = 2$, and $\gamma = 2.5$, such that the values at $\Delta x/\lambda = 8$ are all equal. Using this form, the sensitivity of SI on acoustic resolution can be seen to increase as γ increases. The grazing angle has been set to 20°, and the spectral strength is the second-largest value in Table XYZ.

This comparison is made in Fig. 8, which plots the scintillation index minus a constant C as a function of resolution and spectral exponent. Grazing angle is held constant at 20°, and the second-highest values of spectral strength is used. The constant C was specified so that at $\Delta X/\lambda = 8$, each spectral exponent had the same abcissa on the plot, to better show the difference in slope. SI is least sensitive to ΔX for $\gamma = 1.5$, and most sensitive when $\gamma = 2.5$. This plot contradicts the hypothesis that rms slope at scales greater than the acoustic resolution is the sole driver of intensity fluctuations. Therefore local tilting is not, or not the only cause of heavy-tailed statistics. In the following subsections, we first examine the local tilting hypothesis in greater detail, and then explore other mechanisms that might be driving the SI behavior.

A. Examination of the local tilting hypothesis

We examine the local tilting hypothesis in finer detail first. If this hypothesis is true, then the intensity as a function of space ($I(t)$ mapped to x through $x = -ct/(2\cos(\theta))$ for backscattering), should increase if the large-scale slope at x is negative, and decrease if positive. Consequently there should be a statistical correlation between $I_{\Delta x}(x)$, the intensity at a given resolution at position x, and $s_{\Delta x}(x)$, the slope field low-pass filtered with an upper limit of Δx. This correlation can be quantified in a crude but straightforward manner using the Pearson product moment correlation coefficient, ρ, defined by

$$\rho(s_{\Delta x}, I_{\Delta x}) = \frac{E\left[s_{\Delta x}\left(I_{\Delta x} - E[I_{\Delta x}]\right)\right]}{\sqrt{E\left[s_{\Delta x}^2\right] E\left[\left(I_{\Delta x} - E[I_{\Delta x}]\right)\right]}}, \tag{25}$$

where the slope field is assumed to be a zero-mean process, but intensity is not. This coefficient quantifies the linear variation between a dependent and an independent variable.

We test the hypothesis of local tilting by filtering the slope field at different scales and forming the correlation coefficient with the intensity at a single resolution. The surface filter scale that maximizes the correlation is estimated, and this process is repeated for all acoustic resolutions. The acoustic resolution is ΔX, and the surface filter size is ΔX_{surf}. If the ΔX_{surf} that maximizes ρ, which is denoted $\Delta X_{\max}$, varies in proportion to Δx, then we can conclude 1) that slope modulation is responsible in part for the intensity fluctuations, and 2) slopes at the scale of the acoustic resolution are responsible in part for the fluctuations.

The correlation coefficient for parameters of $\gamma = 2$, $\theta_i = 20°$, and $w = 2 \times 10^{-5}$m is plotted in Fig. 9. ΔX is on the horizontal axis, ΔX_{surf} is on the vertical axis, and ρ is denoted by grayscale. Holding ΔX constant, there is a distinct peak in ρ as a function of

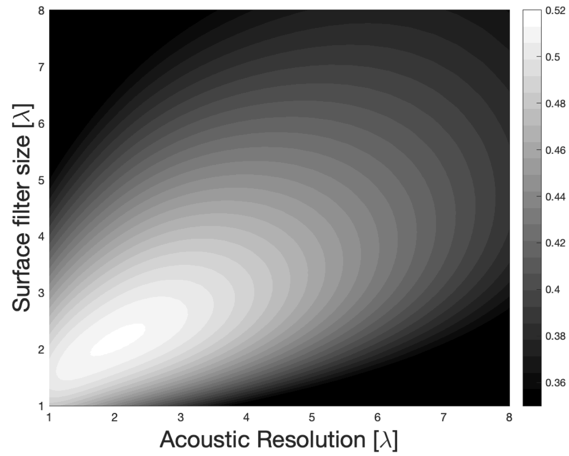

FIG. 9. Correlation coefficient as a function of the acoustic resolution, ΔX, and the surface filter size, ΔX_{surf}.

ΔX_{surf}. The peak value of ρ increases as the acoustic resolution becomes small, indicating that the role of slope modulation is greater for smaller resolution cells. Additionally, the peak in ΔX_{surf} varies with ΔX, indicating the local tilting hypothesis may be correct. This plot has a similar structure for other θ_i, γ, and w.

ΔX_{max}, the value of ΔX_{surf} that maximizes ρ, as a function of ΔX is plotted in Fig. 10. θ_i is constant at 20° grazing angle, each spectral strength is plotted as its own line. The different values of γ appear in subfigures. For each spectral strength and exponent, the maximum slope correlation scale varies monotonically with the acoustic resolution, except for the smallest spectral strength for $\gamma = 1.5$. For $\gamma = 2$, this trend is approximately linear, except for the smallest spectral strength that exhibits a slight negative curvature. The smallest spectral strengths for all values of γ resulted in $SI \approx 1$. For these situations, local tilting is not required to explain the behavior of SI.

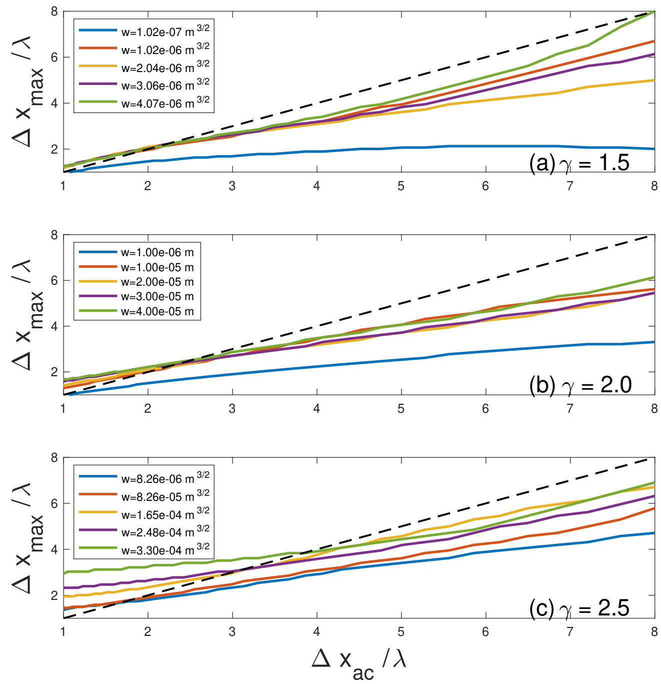

FIG. 10. Surface slope filter scale that maximizes the product moment cross correlation coefficient for each acoustic resolution. Grazing angle has been held constant at 20°, and each line representes a different spectral strength. Each subplot contains a different spectral exponent with (a)$\gamma = 1.5$, (b)$\gamma = 2$, and (c),$\gamma = 2.5$. Dashed black lines have a slope of unity and intercept of zero for reference.

For the other spectral exponents, the dependence of $\Delta X_{\max}$ on ΔX is also mostly linear, but has some negative or positive curvature. A line with unit slope and zero intercept is also plotted for reference. Although there is some departure from linearity, the monotonic dependence of $\Delta X_{\max}$ on ΔX indicates that, to within a proportionality constant, slopes at or larger than the resolution scale account for a significant part of the intensity fluctuations. Since the slopes are generally less than unity, this proportionality constant is less than unity, a result that prompts further study into this effect. This plot provides evidence that the local tilting hypothesis is one component of the intensity fluctuations.

B. Other effects

We have shown through the correlation coefficient that local tilting is in part responsible for the intensity fluctuations, but cannot be the sole origin. The effect of local tilting is modeled physically using the composite roughness approximation (Jackson *et al.*, 1986b; McDaniel and Gorman, 1983), in which the roughness is split into large-scale and small-scale components. Perturbation theory is applied to the small-scale component, and the Kirchhoff approximation to the large-scale component. When the grazing angle is small, the Kirchhoff approximation becomes inaccurate, and multiple scattering and shadowing can become important (Liszka and McCoy, 1982). Based on the analysis in (Thorsos, 1988), shadowing of the incident field is important when the incident grazing angle is comparable to the rms slope angle. Multiple scattering is expected to be important, when the incident or scattered angles are comparable to twice the rms slope angle. Shadowing of the scattered field is important when the scattered grazing angle is comparable to the rms slope angle.

In multiple scattering, the incident field interacts with distant parts of the rough surface (defined as portions outside the resolution cell) multiple times before being radiated back to the acoustic medium (Liszka and McCoy, 1982). Multiple scattering would cause an additive component of the field with a lower amplitude and larger effective ensonified area than the field due to the surface within the resolution cell. If the effective region of multiple scattering were large enough, then scattered field would have contributions from many independent locations, driving the statistics toward a Rayleigh distribution. Coherent combination of the field scattered by the surface roughness located within the resolution cell (including tilting), and the multiply scattered field would then result in a smaller SI than just scattering from within the resolution cell (Johnson *et al.*, 2009; Lyons *et al.*, 2009; Watts, 1987).

Based on the analysis in (Thorsos, 1988, 1990), the Kirchhoff approximation fails due to the presence of multiple scattering when there is significant energy in the roughness spectrum at scales smaller than the wavelength. For power-law surfaces, a surface with a small spectral exponent has more high-frequency energy than one with large spectral exponent. Therefore, simulations with $\gamma = 1.5$ should have more significant multiple scattering than simulations with $\gamma = 2$ or 2.5, and consequently the SI should be lower due to a large effective multiple scattering region. Since we observe this trend in these numerical simulation, we believe that this interpretation based on multiple scattering is a likely cause of the smaller scintillation indicies seen for $\gamma = 1.5$, and a lower sensitivity to the acoustic resolution. At this time, this hypothesis cannot be confirmed more specifically, but requires further research.

Shadowing is also important when the grazing angles become small. A shadowing correction, which is essentially the expected value of the ratio of illuminated to the total surface area, has been derived by (Wagner, 1967). A simplified form of this approximation is widely used in the literature (Jackson *et al.*, 1986b; Thorsos, 1988, 1990) that depends on only grazing angle and rms slope. This approximate form is based on very rough surface, and vanishing correlation length, which seems to be useful for surfaces with a Gaussian roughness spectrum. However the assumption of a vanishing lengths scale is inappropriate for power law spectra, as they exhibit long-range correlation (Mandelbrot and Ness, 1968) when the hurst exponent, $H = (\gamma - 2)/2 > 1/2$. A consequence of long-range correlation is that the local mean tends to a non-zero value, even though its expected value is everywhere zero. Thus if the surface has a local maximum, it may stay below that local maximum for some distance before returning to it. Consequently at low grazing angles, the shadows cast by local maxima can be quite long on power-law surfaces, especially when energy is concentrated in the low-wavenumber portion of the spectra, as it does for large γ. In terms of the scintillation index, the geometric interpreting of shadowing causes parts of the surface to be either illuminated, or not. This binary effect will increase the variance of the intensity, leading to a higher scintillation index. Since we observe much higher scintillation indices for $\gamma = 2.5$ ($H = 3/4$), and these surfaces also have larger rms roughness due to their concentration at low wavenumbers, we believe that shadowing is a likely contributor to the scintillation index. As before, this hypothesis cannot be confirmed here, but requires more detailed analysis.

A physically accurate theoretical model that includes all of these effects is evidently required to predict the scintillation index at low grazing angles. Such a model is, at this time, not available, and is a fruitful opportunity for future research. We have noted that the usual form of the shadowing correction for the intensity may be inappropriate for power-law surfaces, especially when the spectral exponent is large, and the more general version derived in (Wagner, 1967) may be required. The independence of the scattering cross section on resolution established here imposes a useful constraint. Any theoretical model that breaks apart the solution of the exact integral equation into physically interpretable phenomena (such as tilting, shadowing, or multiple scattering) must also satisfy this constraint.

IX. CONCLUSION

In this work Fourier synthesis combined with numerical solution of the Helmholtz integral equation has been performed to analyze the scattered field in terms of the scattering cross section and scintillation index. We have examined the dependence of these two quantities on acoustic resolution to understand the effects that modern high-resolution acoustic imaging systems have on quantitative measurements of seafloor scattering. We have found that for power-law surfaces, the scattering strength is independent of pulse length, which indicates it is a stable quantity to use across measurement systems with different geometries. The scintillation index depends strongly on pulse length. The behavior of SI on pulse length indicates that scattering is fundamentally different in the time and frequency domains, and that further research is needed to understand (or predict) intensity fluctuations in high resolution broadband sonar systems.

Although simulations were performed in two dimensions, these results may be present in three dimensions as well, if the roughness spectrum is assumed to be isotropic. The exact values of the scintillation index will be different for 3D environments, as the rms slope is calculated differently, and out of plane effects may be important.

Heavy-tailed, or non-Rayleigh scattering is commonly observed in scattering measurements and is usually attributed to nonstationary, or patchy environments (Abraham and Lyons, 2004; Lyons *et al.*, 2009). Heavy-tailed statistics have been observed in seemingly homogeneous seafloors by (Lyons *et al.*, 2016), and these numerical simulations have verified that statistically homogeneous surfaces can produce heavy-tailed statistics when interrogated by a broadband high-resolution system. The composite roughness model used in (Lyons *et al.*, 2016) was investigated, and found that it is in part responsible for intensity fluctuations. Other sources of fluctuations, such as shadowing and multiple scattering may be required to fully predict the scattered field. Further research is required to fully understand this aspect of seafloor scattering.

We note a few consequences of heavy-tailed statistics arising in high-resolution systems in homogeneous roughness environments. Heavy-tailed statistics are a significant source of false alarms in acoustic target detection systems. Since scintillation index increases at low angles, long range systems may suffer from decreased performance. The benefit of high resolution systems, more pixels per target, may be offset due to the increased false alarms.

There may be some benefits of resolution dependence of the pdf of the scattered field. Some autofocus algorithms for synthetic aperture systems (e.g. (Blacknell *et al.*, 1992; Callow, 2003; Marston and Plotnick, 2015)), use the scintillation index, or contrast as their cost function. If the acoustic field is entirely due to point scatterers, as is commonly assumed (Brown *et al.*, 2017), then the pdf of the scattered field will be Rayleigh for all resolutions. If an autofocus algorithm is applied, and the point spread function of the imaging algorithm becomes smaller, then the field will still be Rayleigh and contrast will not increase. Therefore, an autofocus algorithm based on SI or lacunarity will not be sensitive to the focus, unless there are discrete scatterers in the scene. However, as show in this paper, SI is a strong function of resolution for homogeneous power law surfaces, especially at low grazing angles. Improving the focus at low grazing angles will lead to an increase in SI, and thus the autofocus algorithm will be more sensitive to the actual degree of focus.

Median filters are often used to "remove" the speckle or intensity fluctuations from acoustic or electromagnetic images before use in remote sensing or target detection algorithms (e.g. (Williams, 2015, 2018) and references therein). Although the scattering cross section, which uses the arithmetic mean of the intensity, is insensitive to resolution, the median is not, since the median is highly dependent on the probability density function. Thus either the cross section can be used as a resolution independent quantity that has a large variance, or its variance can be reduced with the consequence that the pixel intensity will no longer be directly related to scattering strength. Other methods of speckle reduction, such as multilook, must be used if a reliable estimate of scattering strength.

X. ACKNOWLEDGEMENTS

The authors thank the US Office of Naval Research for financial support of this work, as well as the Research Initiation Program of the Naval Postgraduate School. Numerical simulations were performed on the Hamming computing cluster at Naval Postgraduate School.

[1] If phase coding and pulse compression is employed, this analysis deals with the resolution of the compressed, or matched-filtered pulse.

Abraham, D. A., and Lyons, A. P. (**2002**). "Novel physical interpretations of K-distributed reverberation," IEEE J. Ocean Eng. **27**, 800–813.

Abraham, D. A., and Lyons, A. P. (**2004**). "Reverberation envelope statistics and their dependence on sonar bandwidth and scattering patch size," IEEE J. Ocean Eng. **29**, 126–137.

Abramowitz, M., and Stegun, I. A. (**1972**). *Handbook of Mathematical Functions* (Dover, Mineola, NY).

Anderson, E., Bai, Z., Bischof, C., Blackford, S., Demmel, J., Dongarra, J., Croz, J. D., Greenbaum, A., Hammarling, S., McKenney, A., and Sorensen, D. (**1999**). *LAPACK Users' Guide*, 3rd ed. (SIAM, Philadelphia,PA).

Atkinson, K. (**1997**). *The Numerical Solution of Integral Equations of the Second Kind* (Cambridge University Press, Cambridge, UK).

Bellettini, A., and Pinto, M. (**2009**). "Design and experimental results of a 300-khz synthetic aperture sonar optimized for shallow-water operations," IEEE J. Ocean Eng. **34**(3), 285–293.

Blacknell, D., Blake, A. P., Oliver, C. J., and White, R. G. (**1992**). "A comparison of sar multilook registration and contrast optimisation autofocus algorithms applied to real sar data," in *92 International Conference on Radar*, pp. 363–366.

Brown, D. C., Johnson, S. F., and Olson, D. R. (**2017**). "A point-based scattering model for the incoherent component of the scattered field," J. Acoust. Soc. Am. **141**(3), EL210–EL215, doi: 10.1121/1.4976584.

Callow, H. J. (**2003**). "Signal processing for synthetic aperture sonar image enhancement," Ph.D. thesis, University of Canterbury, Christchurch, New Zealand.

Devaney, A. J. (**2012**). *Mathematical Foundations of Imaging, Tomography, and Wavefield Inversion* (Cambridge University Press, Cambridge, UK).

Dillon, J. (**2018**). "Real-time interferometric sas processing with ultra-low power consumption," in *OCEANS 2018 MTS/IEEE Charleston*, pp. 1–6, doi: 10.1109/OCEANS.2018.8604512.

Fossum, T. G., Sæbø, T. O., Langli, B., Callow, H., and Hansen, R. E. (**2008**). "HISAS 1030 - High resolution interferometric synthetic aperture sonar," in *Proc. Can. Hydrog. Conf.*, Victoria BC, Canada.

Gauss, R. C., Fialkowski, J. M., Henyey, F. S., Ogden, P. M., Reilly, S. M., Sundvik, M. T., and Thorsos, E. I. (**1996**). "Reassessing the issue of pulse-length dependence of bottom scattering strengths in Critical Sea Test data," Report , http://www.dtic.mil/docs/citations/ADA321988.

Hackbusch, W. (**2015**). *Hierarchical Matrices: Algorithms and Analysis*, 1st ed. (Springer Publishing Company, Incorporated).

Hefner, B. T. (**2015**). "Inversion of high frequency acoustic data for sediment properties needed for the detection and classification of uxos," Final Report , https://www.serdp-estcp.org/content/download/34593/333838/file/MR-2229-FR.pdf.

Hellequin, L., Boucher, J. M., and Lurton, X. (**2003**). "Processing of high-frequency multibeam echo sounder data for seafloor characterization," IEEE J. Ocean Eng. **28**(1), 78–89, doi: 10.1109/JOE.2002.808205.

Henyey, F. S., Thorsos, E. I., and Nathwani, K. M. (**1995**). "Scattering strength cannot depend on the length of a pulse," J. Acoust. Soc. Am. **98**(5), 2986–2987, doi: http:

//dx.doi.org/10.1121/1.413926.

Ishimaru, A. (**1978**). *Wave Propagation and Scattering in Random Media*, **2** (Academic Press).

Jackson, D. R., Baird, A. M., Crisp, J. J., and Thomson, P. A. G. (**1986**a). "High-frequency bottom backscatter measurements in shallow water," J. Acoust. Soc. Am. **80**(4), 1188–1199, doi: http://dx.doi.org/10.1121/1.393809.

Jackson, D. R., and Richardson, M. D. (**2007**). *High-Frequency Seafloor Acoustics*, 1st ed. (Springer, New York, NY).

Jackson, D. R., Winebrenner, D. P., and Ishimaru, A. (**1986**b). "Application of the composite roughness model to high-frequency bottom backscattering," J. Acoust. Soc. Am. **79**, 1410–1422.

Jakeman, E. (**1980**). "On the statistics of K-distributed noise," J. Phys. A: Math. Gen. **13**, 31–48.

Johnson, S. F., Lyons, A. P., and Abraham, D. A. (**2009**). "Ieee j. ocean eng.," IEEE Journal of Oceanic Engineering **34**(4), 476–484, doi: 10.1109/JOE.2009.2032794.

Liszka, E. G., and McCoy, J. J. (**1982**). "Scattering at a rough boundary - extensions of the kirchhoff approximation," J. Acoust. Soc. Am. **71**, 1093–1100.

Liu, Y., ed. (**2009**). *Fast Multipole Boundary Element Method: Thory and Applications in Engineering* (Cambridge University Press, Cambridge, UK).

Lupien, V. (**1999**). "The role of scale structure in scattering from random rough surfaces," J. Acoust. Soc. Am. **105**, 2187–2202.

Lyons, A. P., Abraham, D. A., and Johnson, S. F. (**2010**). "Modeling the effect of seafloor ripples on synthetic aperture sonar speckle statistics," IEEE J. Ocean Eng. **35**(2), 242–249, doi: 10.1109/JOE.2009.2039656.

Lyons, A. P., Johnson, S. F., Abraham, D. A., and Pouliquen, E. (**2009**). "High-frequency scattered envelope statistics of patchy seafloors," IEEE J. Ocean Eng. **34**, 451–458.

Lyons, A. P., Olson, D. R., and Hansen, R. E. (**2016**). "Quantifying the effect of random seafloor roughness on high-frequency synthetic aperture sonar image statistics.," in *Proc. Inst. Acoust. Conf.: Acoustic and Environmental Variability, Fluctuations and Coherence*, Cambridge, UK.

Lysanov, Y. P. (**1973**). "A property of the scattering coeffciient in the fraunhofer zone," Sov. Phys. Acoust. **18**, 505 – 506.

Mandelbrot, B. B., and Ness, J. W. V. (**1968**). "Fractional brownian motions, fractional noises and applications," SIAM Review **10**(4), 422–437, http://www.jstor.org/stable/2027184.

Marston, T. M., and Plotnick, D. S. (**2015**). "Semiparametric statistical stripmap synthetic aperture autofocusing," IEEE Transactions on Geoscience and Remote Sensing **53**(4), 2086–2095, doi: 10.1109/TGRS.2014.2353515.

McDaniel, S. T., and Gorman, A. D. (**1983**). "An examination of the composite-roughness scattering model," J. Acoust. Soc. Am. **73**, 1476–1486.

Olson, D. R., Lyons, A. P., Abraham, D. A., and Sæbø, T. O. (**2019**). "Scattering statistics of rock outcrops: Model-data comparisons and bayesian inference using mixture distributions," J. Acoust. Soc. Am. **145**(2), 761–774, doi: 10.1121/1.5089892.

Olson, D. R., Lyons, A. P., and Sæbø, T. O. (**2016**). "Measurements of high-frequency acoustic scattering from glacially eroded rock outcrops," J. Acoust. Soc. Am. **139**(4), 1833–1847, doi: 10.1121/1.4945589.

Oppenheim, A. V., Schafer, R. W., and Buck, J. R. (**1999**). *Discrete-time Signal Processing (2nd Ed.)* (Prentice-Hall, Inc., Upper Saddle River, NJ, USA).

Pinto, M. (). "Interferometric synthetic aperture sonar design optimized for high area coverage shallow water bathymetric survey," in *Proc. 4th Int. Conf Exhib. Underwater Ac. Meas.*, Kos, Greece, pp. 505–512.

Sauter, S. A., and Schwab, C. (**2011**). *Boundary Element Methods* (Springer-Verlag, Heidelberg).

Sternlicht, D. D., Fernandez, J. E., Prater, J. L., Weaver, J. N., Isaacs, J. C., Montgomery, T. C., Loeffler, C. M., and Purcell, M. (**2016**). "Advanced sonar technologies for high clearance rate mine countermeasures," in *OCEANS 2016 MTS/IEEE Monterey*, pp. 1–8, doi: 10.1109/OCEANS.2016.7761133.

Tatarski, V. I. (**1961**). *Wave Propagation in a Turbulent Medim* (Dover Reprint, New York).

Thorsos, E. I. (**1988**). "The validity of the Kirchhoff approximation for rough surface scattering using a Gaussian roughness spectrum," J. Acoust. Soc. Am. **83**, 78–92.

Thorsos, E. I. (**1990**). "Acoustic scattering from a "Pierson-Moskowitz" sea surface," J. Acoust. Soc. Am. **88**(1), 335–349, doi: 10.1121/1.399909.

Toporkov, J., Marchand, R., and Brown, G. (**1998**). "On the discretization of the integral equation describing scattering by rough conducting surfaces," Antennas and Propagation, IEEE Transactions on **46**(1), 150 –161, doi: 10.1109/8.655462.

Wagner, R. J. (**1967**). "Shadowing of randomly rough surfaces," J. Acoust. Soc. Am. **41**, 138 – 147.

Wang, Z., and Bovik, A. C. (**2002**). "A universal image quality index," IEEE Signal Processing Letters **9**(3), 81–84, doi: 10.1109/97.995823.

Wang, Z., Bovik, A. C., Sheikh, H. R., and Simoncelli, E. P. (**2004**). "Image quality assessment: from error visibility to structural similarity," IEEE Transactions on Image Processing **13**(4), 600–612, doi: 10.1109/TIP.2003.819861.

Watts, S. (**1987**). "Radar detection prediction in k-distributed sea clutter and thermal noise," IEEE Trans. Aerosp. Electron. Sys. **23**(1), 40–45.

Williams, D. P. (**2015**). "Fast unsupervised seafloor characterization in sonar imagery using lacunarity," IEEE Transactions on Geoscience and Remote Sensing **53**(11), 6022–6034, doi: 10.1109/TGRS.2015.2431322.

Williams, D. P. (**2018**). "The Mondrian detection algorithm for sonar imagery," IEEE Transactions on Geoscience and Remote Sensing **56**(2), 1091–1102, doi: 10.1109/TGRS.2017.2758808.

Williams, K., Jackson, D., Thorsos, E., Tang, D., and Briggs, K. (**2002**). "Acoustic backscattering experiments in a well characterized sand sediment: Data/model comparisons using sediment fluid and Biot models," IEEE J. Ocean Eng. **27**, 376–387.

Williams, K. L., and Jackson, D. R. (**1998**). "Bistatic bottom scattering: Model, experiments, and model/data comparison," J. Acoust. Soc. Am. **103**(1), 169–181, doi: 10.1121/1.421109.

Winebrenner, D., and Ishimaru, A. (**1986**). "On the far-field approximation for scattering from randomly rough surfaces," Antennas and Propagation, IEEE Transactions on **34**(6), 847–849, doi: 10.1109/TAP.1986.1143901.

Wu, T. W., ed. (**2000**). *Boundary Element Acoustics: Fundamentals and Computer Codes* (WIT Press, Southampton, UK).